Supplementary Materials: Assessing the Long-Term Behaviour of the Industrial Bentonites Employed in a Repository for Radioactive Wastes by Studying Natural Bentonites in the Field

W. Russell Alexander, Heini M. Reijonen, Gillian MacKinnon, Antoni E. Milodowski, Alistair F. Pitty and Andreas Siathas

1. Kato Moni Core Sub-Sampling Details and Analytical Plan by Laboratory

Table S1. Kato Moni core sub-sampling and analytical plan.

Sample	Depth (m)	BGS CEC	BGS Optical	BGS SEM	BGS Stable Isotopes	BGS Palaeo-Dating	SUERC NDS	Geoinvest Physical Properties	DIA XRD & Density	Uni Helsinki Hyperspec
KM1										
L1	0.55–0.59		x		x	x	x			
L2	8.30–8.35				x	x			density	
L2–1	8.35–8.40									
B1+	8.40–8.55							x		
B1	8.55–8.65	x	x			x	x			
B1-sub	8.55–8.65								x	
B2a	8.77–8.8	x	x	x			x			
B2-sub	8.84–8.85								x	
B3	9.00–9.07	x	x	x			x			
B3-sub	9.07–9.08								x	
B3-1	9.08–9.17							x		
B3-2	9.17–9.30							x		
B3-3	9.50–9.60							x		
B4	9.60–9.70	x	x	x			x			
B4-sub B4-hyper	9.70–9.76								x	x
B4-1	9.80–10.10							x		
B5	10.10–10.20		x	x						
B5-1	10.20–10.42							x		
B6	10.50–10.60		x	x						
B6-1	10.60–10.70							x		
B6-2	10.84–11.16							x		
B6-3	11.16–11.55							x		
B7	11.55–11.61	x	x	x			x			
KM2										
B1	13.50–13.55	x				x	x			

Sample	Depth (m)	BGS CEC	BGS Optical	BGS SEM	BGS Stable Isotopes	BGS Palaeo-Dating	SUERC NDS	Geoinvest Physical Properties	DIA XRD & Density	Uni Helsinki Hyperspec
B1-sub	13.50–13.55								**x**	
B2	13.55–13.65	**x**								
B3	13.65–13.80	**x**	**x**	**x**		**x**	**x**			
B3-sub	13.80–13.82								**x**	
B3-1	13.82–14.05							**x**		
B3-2	14.20–14.40							**x**		
B4	14.50–14.65	**x**	**x**	**x**			**x**			
B4-sub	14.79–14.80								**x**	
B4-hyper	14.65–14.80									**x**
B5	14.90–15.00		**x**	**x**	**x**					
B6	15.50–15.55		**x**	**x**			**x**			
B6-sub	15.55–15.56								**x**	
B7	15.98–16.08	**x**	**x**	**x**	**x**		**x**			
B7-sub	16.08–16.20								**x**	
KM3a										
B1	0.17–0.24	x	x	x			x			
B1-sub	0.24–0.25								x	
B1-hyper	0.25–0.35									x
B1-1	0.35–0.54							x		
B2	0.54–0.55	x	x	x		x	x			
B2-sub	0.53–0.54								x	
B3	0.82–0.92	x	x	x			x			
B3-sub	0.92–0.93								x	
B3-1	0.95–1.30							x		
B3-2	1.30–1.52							x		
B4	1.52–1.58	x	x	x						
B4-1	1.70–1.84							x		
B4-2	1.84–1.97							x		
B5	2.00–2.10		x	x			x			
B5-sub	2.10–2.11								x	
B5-hyper	2.11–2.19									x
B5-1	2.20–2.26							x		
B5-2	2.26–2.44							x		
B5-3	2.44–2.80							x		
B6	2.80–2.90		x	x						
KM3b										
B7	4.20–4.65	x	x	x						
B7-sub	4.20–4.65								x	

2. XRF Extracted Qualitative Data

Table S2. XRF extracted qualitative data (wt %) for cores KM1, KM2, KM3 and KM3a from the Kato Moni site, Cyprus.

Borehole	Sample	Depth (Upper)	Base of Limestone	Depth from Limestone	SiO_2	Fe_2O_3	CaO	Al_2O_3	MgO	K_2O	TiO_2	Na_2O	MnO	SrO
KM1	B1	8.55	8.55	0.00	42	15.8	17.9	13.4	6.05	1.75	1.25	1.33	0.161	0.0741
KM1	B2-sub	8.84	8.55	0.29	32.6	12.9	34.8	10.3	5.29	1.42	1.09	0.966	0.141	0.0979
KM1	B3-sub	9.07	8.55	0.52	45	17.1	11.9	14.7	6.01	1.9	1.29	1.5	0.145	0.0738
KM1	B4-sub	9.70	8.55	1.15	41.8	15	18.8	13.8	5.49	1.85	1.37	1.29	0.135	0.0864
KM1	B7sub	11.61	8.55	3.06	44.9	14.4	14.8	14.6	5.82	2.12	1.41	1.37	0.166	0.0916
KM2	B1	13.50	13.50	0.00	43.4	16.7	15	14.1	5.82	1.82	1.36	1.22	0.207	0.076
KM2	B3-sub	13.80	13.50	0.30	41.8	14.2	19.6	13.6	5.8	1.94	1.39	1.1	0.163	0.0819
KM2	B4-sub	14.79	13.50	1.29	41.2	16.2	18.3	14.2	5.25	1.84	1.22	1.24	0.151	0.0925
KM2	B6-sub	15.55	13.50	2.05	44.5	14.4	15.1	14.9	5.64	2.03	1.43	1.34	0.14	0.184
KM2	B7-sub	16.08	13.50	2.58	40.2	16.9	19.3	13.6	4.88	1.77	1.34	1.28	0.122	0.231
KM3a	B1-sub	0.24	0.00	0.24	49.6	9.68	17.1	13.4	4.88	2.07	0.992	0.964	0.541	0.0909
KM3a	B2-sub	0.53	0.00	0.53	46.7	8.56	18.1	12.6	4.33	2.03	0.924	0.691	4.77	0.113
KM3a	B3-sub	0.92	0.00	0.92	49.7	9.14	17.3	13.7	4.36	2.12	0.974	1.07	0.623	0.101
KM3a	B5-sub	2.10	0.00	2.10	58.7	11.9	1.35	16.7	4.53	2.91	1.11	1.56	0.3	0.0702
KM3a	B7-sub	4.20	0.00	4.20	57.6	11.6	1.35	18.3	4.3	2.32	1.06	1.17	1.43	0.0538
Borehole	**Sample**	**Depth (Upper)**	**Base of Limestone**	**Depth from Limestone**	**Cl**	**SO_3**	**ZrO_2**	**P_2O_5**	**ZnO**	**NiO**	**CuO**	**Cr_2O_3**	**Rb_2O**	**V_2O_5**
KM1	B1	8.55	8.55	0.00	0.0407	0.0627	0.0235	0.0545	0.0194	0.0178	0.0163	0.0214	0.00776	
KM1	B2-sub	8.84	8.55	0.29	0.0385	0.0717	0.0271	0.0448	0.0171	0.0121	0.0106	0.0297	0.00557	0.085
KM1	B3-sub	9.07	8.55	0.52	0.0403	0.0689	0.0246	0.0692	0.0241	0.0172	0.016	0.0205	0.00679	0.0808
KM1	B4-sub	9.70	8.55	1.15	0.034	0.0554	0.0294	0.0638	0.0246	0.0133	0.0175	0.0228	0.00771	0.0909
KM1	B7sub	11.61	8.55	3.06	0.0343	0.0816	0.0284	0.0671	0.02	0.0125	0.0164		0.00784	0.0833
KM2	B1	13.50	13.50	0.00	0.0224	0.0467	0.0253	0.0667	0.023	0.0161	0.0192		0.00734	0.0986
KM2	B3-sub	13.80	13.50	0.30	0.0192	0.0511	0.0264	0.0592	0.0239	0.0126	0.0172		0.00651	0.104
KM2	B4-sub	14.79	13.50	1.29	0.0158	0.0508	0.0269	0.0586	0.0224	0.0138	0.0161	0.0285	0.00772	
KM2	B6-sub	15.55	13.50	2.05	0.0166	0.0832		0.0583	0.022	0.00973	0.0193		0.0066	
KM2	B7-sub	16.08	13.50	2.58	0.0223	0.0952		0.069	0.0218	0.0142	0.0165	0.0234	0.00677	0.0707
KM3a	B1-sub	0.24	0.00	0.24	0.0966	0.104	0.0176	0.278	0.024	0.0282	0.0159	0.035	0.0123	0.0406
KM3a	B2-sub	0.53	0.00	0.53	0.143	0.131	0.016	0.259	0.0272	0.0966	0.0693	0.0334	0.0119	0.0681
KM3a	B3-sub	0.92	0.00	0.92	0.24	0.195	0.0155	0.273	0.021	0.0278	0.0168	0.0392	0.0114	
KM3a	B5-sub	2.10	0.00	2.10	0.152	0.139	0.0179	0.329	0.025	0.034	0.0177	0.0424	0.0135	
KM3a	B7-sub	4.20	0.00	4.20	0.17	0.15	0.0269	0.316	0.0234	0.0325	0.0271	0.0273	0.0126	0.0583

3. APFU and AFM Triaxial Plots for Boreholes KM2 and KM3 and Detailed Petrographic Observations for Boreholes KM1, KM2 and KM3

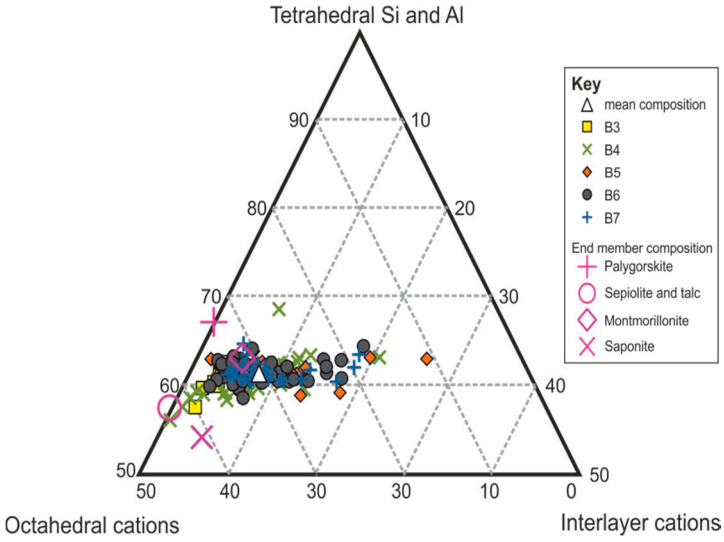

Figure S1. Triaxial Si—octahedral cations—interlayer cations plot using APFU values. Data from KM2. All clay data is colour coded by sample. End member palygorskite, sepiolite, talc, montmorillonite and saponite points included for reference.

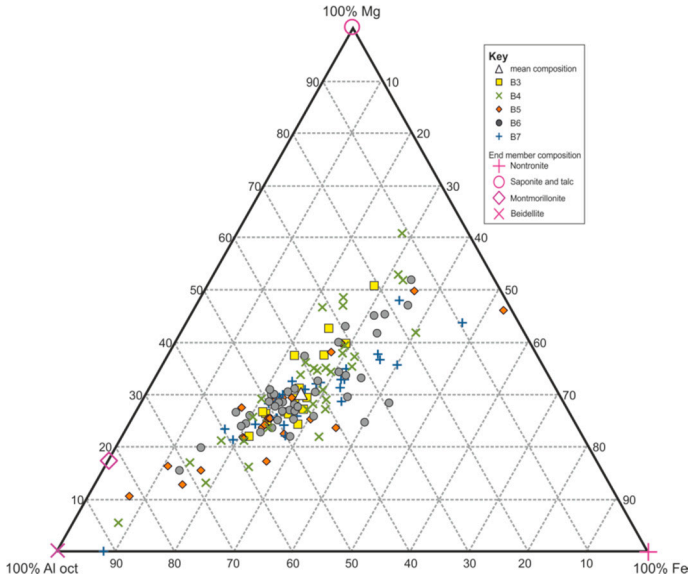

Figure S2. Triaxial octahedral Al–Fe–Mg cations plot using APFU values. Data from KM2. All clay data colour coded by sample. End member nontronite, beidellite, talc, saponite and montmorillonite points included for reference.

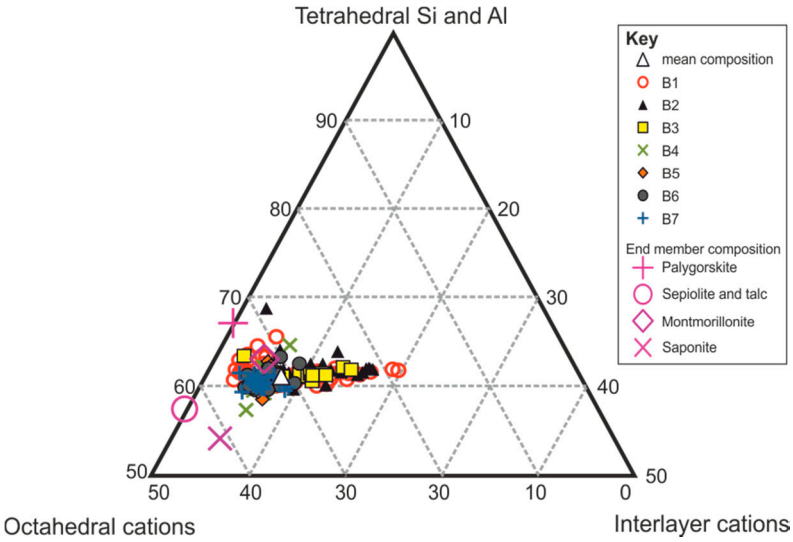

Figure S3. Triaxial Si—octahedral cations—interlayer cations plot using APFU values. Data from KM3. All clay data is colour coded by sample. End member palygorskite, sepiolite, talc, montmorillonite and saponite points included for reference.

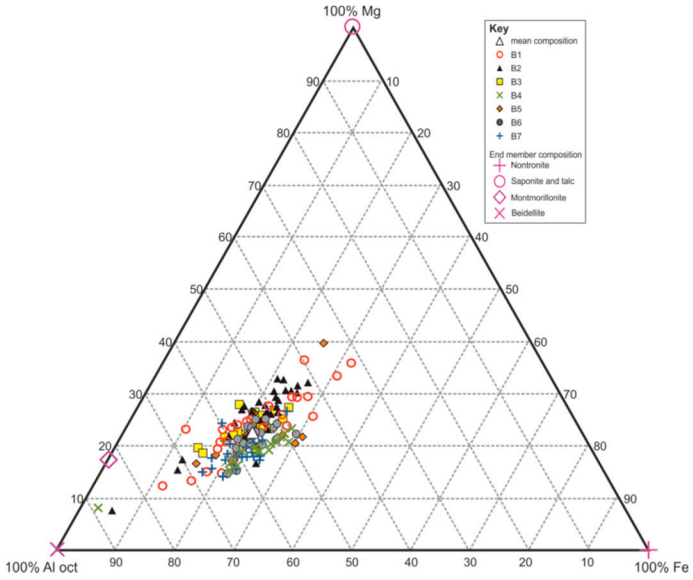

Figure S4. Triaxial octahedral Al–Fe–Mg cations plot using APFU values. Data from KM3. All clay data colour coded by sample. End member nontronite, beidellite, talc, saponite and montmorillonite points included for reference.

Detailed Petrographic Observations on a Sample-by-Sample Basis:

3.1. KM1 L1

3.1.1. Hand Sample

This sample is from the top of the limestone, depth 0.55–0.59 m. The sample was a light cream colour, and a hard, coherent sample which cut without breakage. There are distinct, sub-horizontal, sinuous fractures across the width of the thin section. There are no macro-fossil fragments present.

Plate C1. Photographs of the hand sample: left, before cutting, right, after cutting.

3.1.2. Optical Observations

The sample comprises a micritic limestone: no fossils are present. Clear fractures are present throughout the sample, and the blue dye has penetrated some distance either side of these fractures indicating the material alongside the fractures is permeable. Some fractures indicate some secondary mineralisation. There is a high degree of porosity in the sample indicated by the blue dye, which has given a speckled or 'polka-dotted' appearance to the section (Plate C3). Each patch of blue dye contains a clear microfracture at its centre (Plate C4).

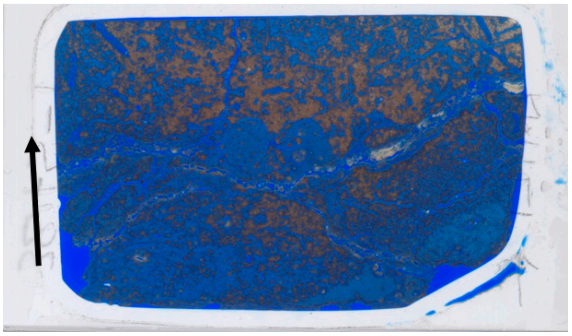

Plate C2. Scanned image of the thin section showing a contrast between highly porous material and denser, non-porous material.

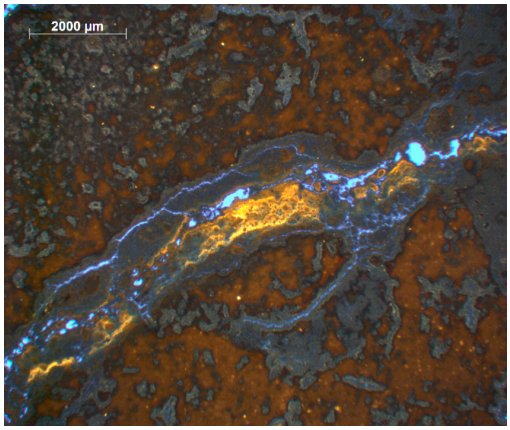

Plate C3. An optical micrograph in PPL showing the 'polka-dot' texture due to the uneven porosity, and a fracture with possible secondary mineralisation.

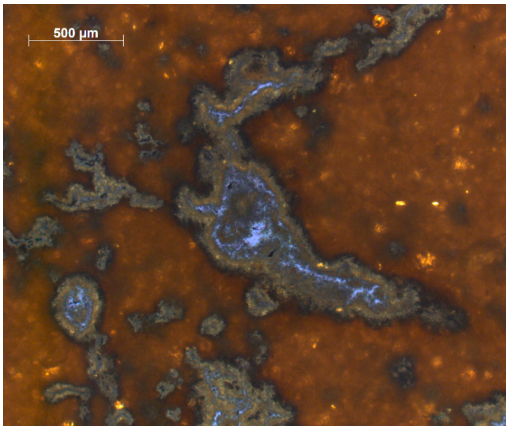

Plate C4. A PPL image showing detail of the porosity. Each patch of porosity contains a microfracture at its centre.

3.1.3. SEM Analysis

This sample is an argillaceous limestone, formed from calcium carbonate micrite. The section has a mottled appearance due to the combination of unaltered calcium carbonate, and an alteration phase, which EDAX spectra indicates is rich in Mg and Si. This Mg/Si phase surrounds the microfractures. Some secondary precipitation of calcium carbonate is present within the fractures and this may be due to remobilisation and re-precipitation of calcium carbonate with a dendritic texture. The presence of hollow spheres within the secondary material may indicate that some of this precipitation could be due to carbonation following microbial or organic activity.

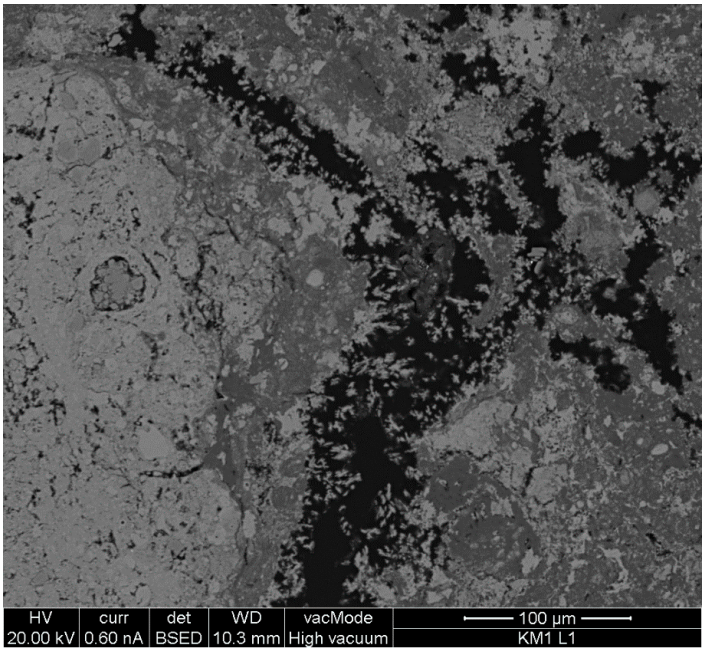

Plate C5. BSEM image of sample KM1 L1 showing a microfracture (**black**) surrounded by calcium carbonate (**light grey**) and an Mg–Si alteration phase (**mid-grey**).

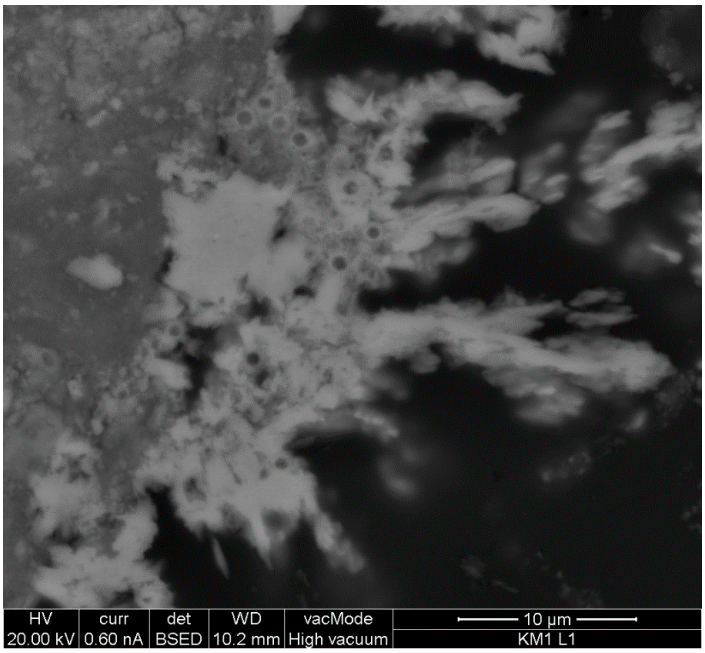

Plate C6. BSEM image showing detail of the secondary calcium carbonate which lines the microfracture, and shows dendritic-type growth. The presence of some hollow spheres probably indicates some of this may be due to carbonation of microbial or organic activity.

3.2. KM1 B1

3.2.1. Hand Sample

This sample was highly fragmented (Plate C7), and one of the larger pieces was used for thin sectioning. The matrix of the sample is fine-grained, appears homogenous and is highly fissile.

Plate C7. Photograph of the hand sample prior to sampling for analysis, showing the fragmented nature of the sample.

3.2.2. Optical Observations

The matix is dense, with numerous fossils (e.g., foraminifera) present. Some evidence of burial compaction (e.g., shattered grains) is visible within the sample. The fractures are clean, pull apart fractures with no evidence for secondary mineralisation. These fractures may be artefacts of the thin section process (e.g., dessication).

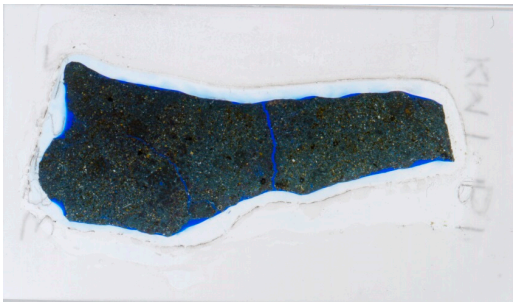

Plate C8. Scanned image of the thin section. Note: due to the fragmented nature of the sample, no orientation could be recorded.

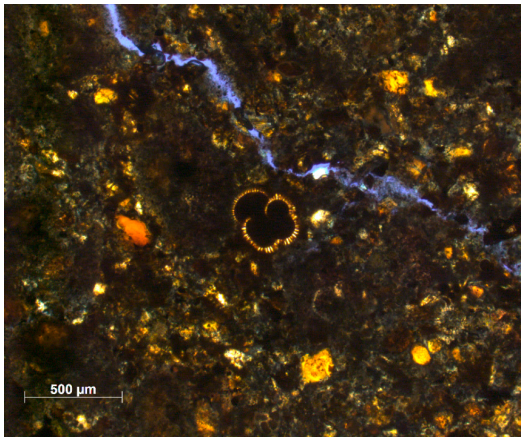

Plate C9. PPL image of sample showing the dense nature of the matrix, a foraminifera, and microfracture. There is no evidence for secondary precipitation.

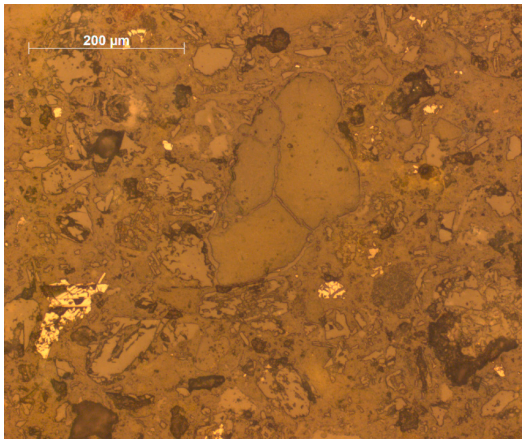

Plate C10. Reflected light image showing evidence of burial compaction in the central grain which has been shattered in-situ.

3.2.3. SEM Analysis

The matrix of this sample is very dense and tightly packed. The fractures are clean, pull-apart fractures with no evidence of secondary precipitation (Plate C11). Some sinoidal fractures highlight pre-existing pellets within the matrix which are probably pelloids (Plate C12). There is evidence of minor mobilisation of Fe in some areas of the sample.

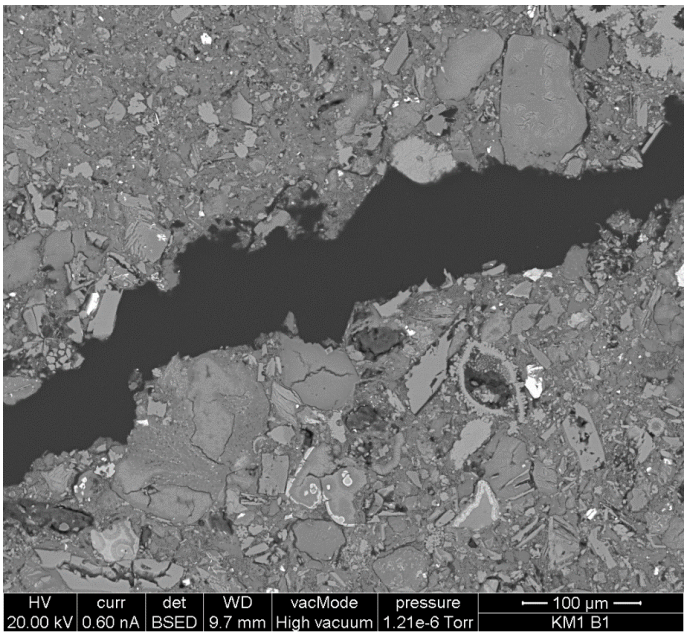

Plate C11. BSEM image of a fracture showing the well-defined pull-apart nature of the break. There is no evidence of secondary precipitation.

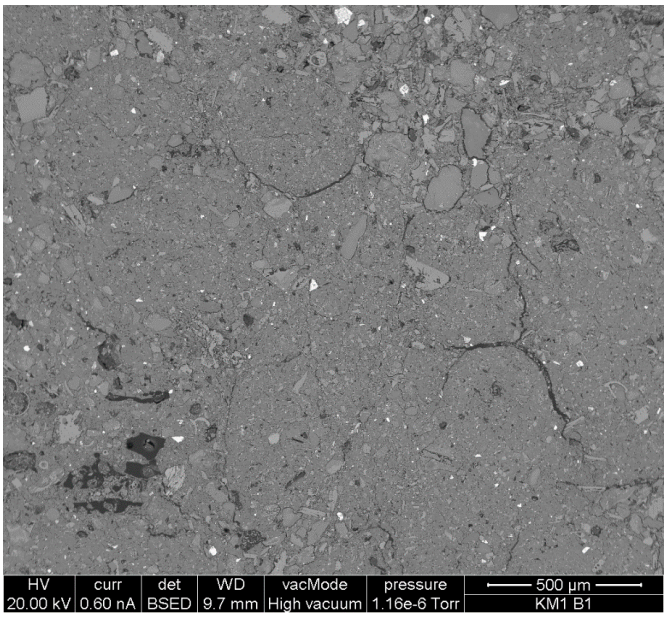

Plate C12. BSEM image showing sinuous fractures appearing. These highlight pre-existing pellets within the matrix.

3.3. KM1 B2a

3.3.1. Hand Sample

This is a light-brown coloured, fine-grained, homogenous sample which is highly fractured but remained reasonably cohesive during cutting.

Plate C13. Photograph of the hand sample prior to cutting and sampling.

3.3.2. Optical Observations

The sample is cross-cut throughout with sharp, angular pull-apart fractures. Material within larger fractures has been pulverised (Plate C15). No evidence of secondary precipitation was observed optically. Numerous fossil fragments are present in the matrix. The matrix comprises some very dense material which contrasts to more porous material (Plate C16).

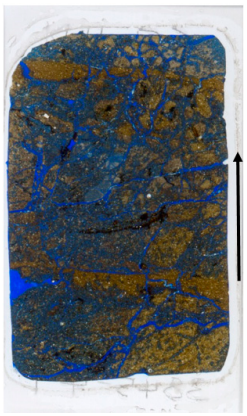

Plate C14. Scanned image of the thin section showing way-up orientation.

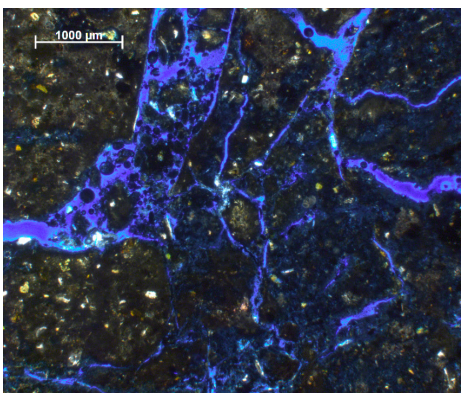

Plate C15. PPL image showing the shattered sample with the angular nature of the fractures. Material within the larger fractures has been pulverised.

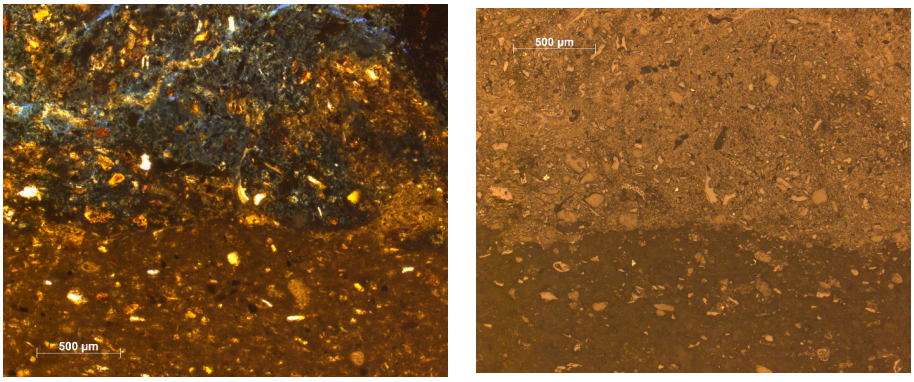

Plate C16. Above **left**: PPL image showing the contract between dense, low-porosity material and high porosity material; Above **right**: the same field of view in reflected light which clearly shows the difference between the two materials.

3.3.3. SEM Analysis

BSEM imaging highlights the presence of pelloidal textures on the microscale which show some chemical differences. EDXA spectra indicate that the less dense matrix contains minor Na, whereas the pelloids contain slightly higher Mg and a lack of Na (Plate C17). Some minor mobilisation of Fe is present.

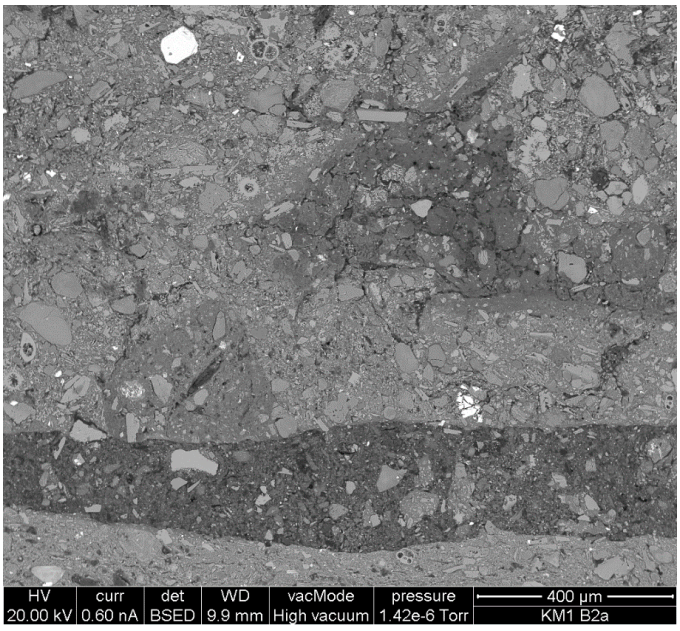

Plate C17. BSEM image showing chemical contrasts between a highly porous fracture (darkest area) and more Mg-rich material in a pelloid (bottom left quadrant). This Mg-rich material also lines the more porous area in the upper right quadrant. The light grey matrix contains lower Mg and higher Na.

3.4. KM1 B3

3.4.1. Hand Sample

This is a mid-brown coloured, fine-grained, homogenous sample which is highly fractured but remained reasonably cohesive during splitting. Following splitting, the resulting surface texture was relatively rough.

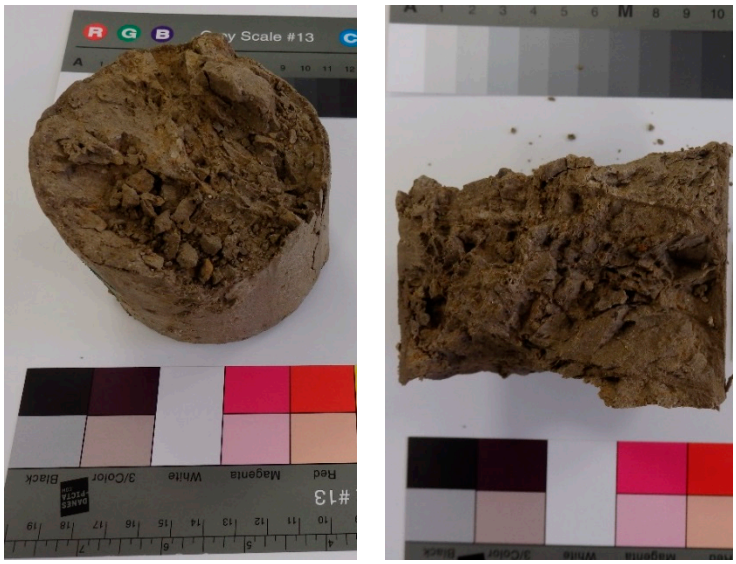

Plate C18. Photograph of the hand sample, **Left**: prior to splitting and sampling; **Right**: sample after splitting showing the internal structure.

3.4.2. Optical Observations

Porosity is variable within this sample as indicated by the blue dye. Some fractures are clean and angular, whereas the majority are thin, sinuous fractures with increased porosity on either side of the fracture (Plate C20). There is no evidence of secondary precipitation. The matrix is also of variable density, fine grained with numerous fossil fragments (e.g., shell fragments and foraminifera). The denser material which has not been stained with blue dye is very fine grained (Plate C21).

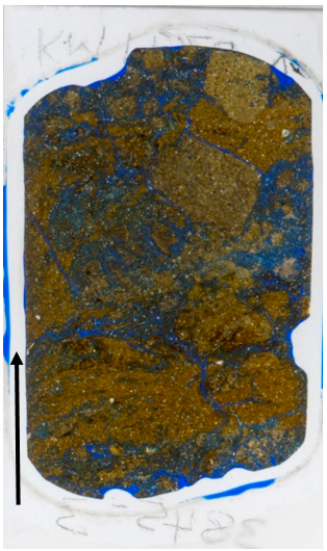

Plate C19. Scanned image of the thin section showing way-up orientation.

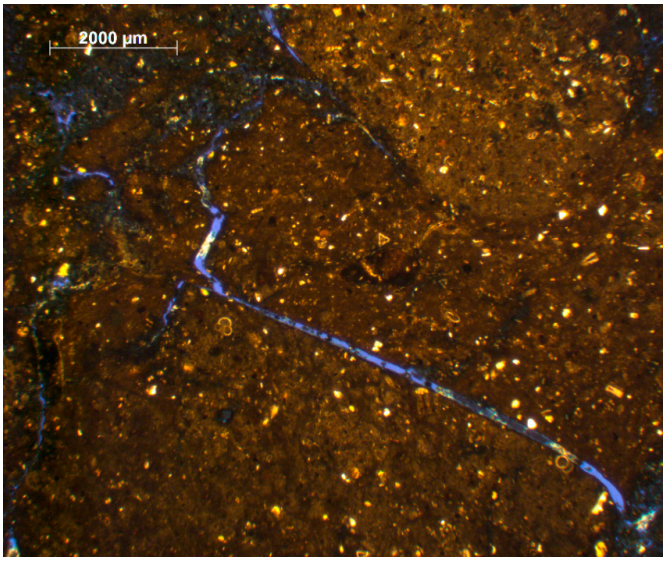

Plate C20. PPL image showing a clean, angular fracture across the centre of the image, and thin, sinuous fracture in the top left quadrant. The thin, sinuous fractures have increased porosity in the material either side of the fracture.

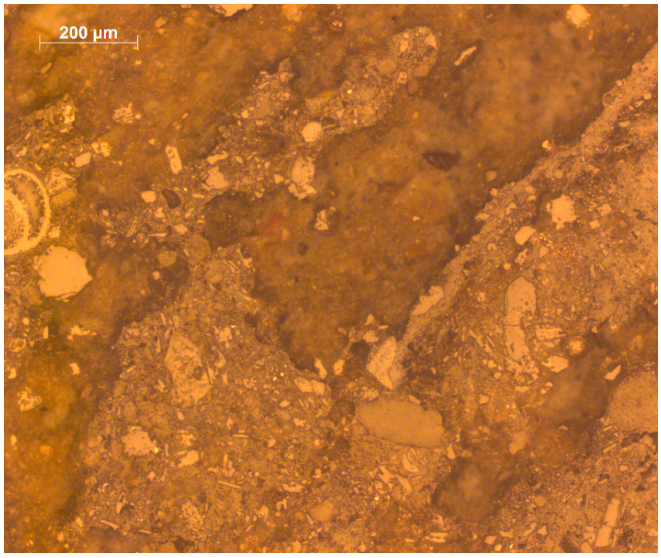

Plate C21. Reflected light image showing the contrast within the matrix. The very fine grained material (darker brown in this image) has not been stained with blue dye, indicating a lack of porosity. In contrast, the coarser material has a higher degree of porosity and has been stained with blue dye.

3.4.3. SEM Analysis

The sample revealed less contrast within the sample than indicated under the optical microscope, although a slight variation is present in the matrix. Slightly coarser material contains a higher porosity and degree of microfractures, whereas the slightly finer-grained material is denser and more coherent. Coarser clasts are present throughout both variations of matrix.

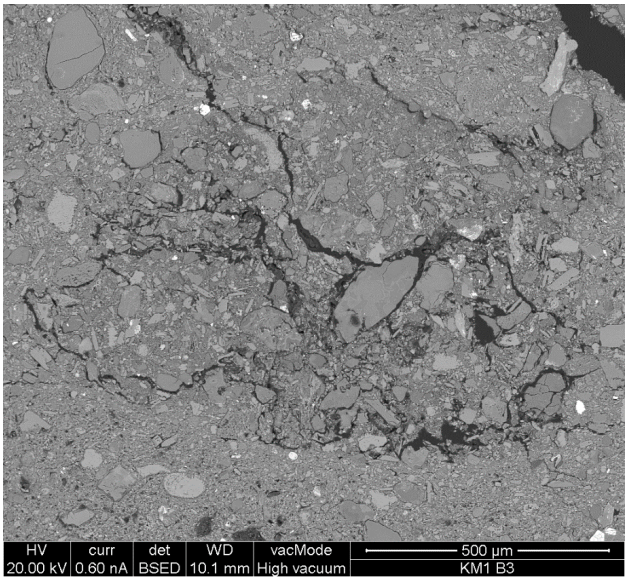

Plate C22. BSEM image showing slightly coarser, more porous material with finer-grained denser material. Coarser clasts are present within both types of matrix.

3.5. KM1 B4

3.5.1. Hand Samples

A dense, mid brown, coherent sample of homogenous appearance. The sample remained cohesive when broken apart, and the resulting surface texture was relatively smooth.

Plate C23. Photographs of the hand sample. **Left**: the sample prior to splitting; **Right**: half of the split sample showing the internal texture.

3.5.2. Optical Observations

Two major sub-horizontal fractures cross cut the section, from which numerous, angular, minor fractures originate. The fractures appear clean with no evidence of secondary precipitation. Blue dye has penetrated some distance into the matrix on either side of the fractures indicating a slight increase in porosity surrounding the fractures (Plate C25). The matrix is dense with some slight variations in

density indicated under reflected light. Some fossil fragments and micro-fossils are present within the matrix (Plate C26).

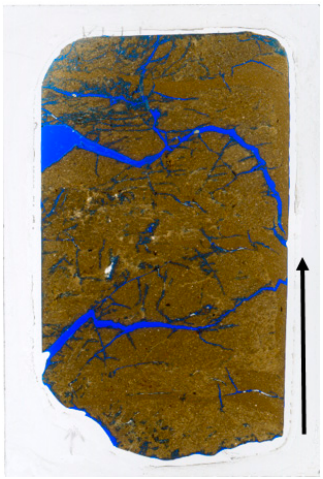

Plate C24. Scanned image of the thin section showing way-up orientation.

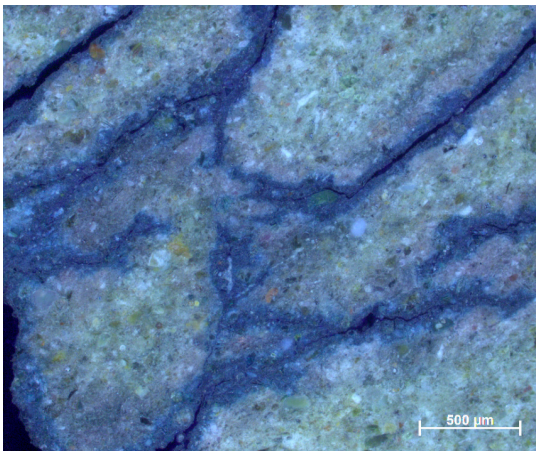

Plate C25. Dark-field image showing part of the fracture network. This image clearly shows the extent of blue-dye penetration either side of a fracture indicating a slight increase in porosity within the proximity of a fracture.

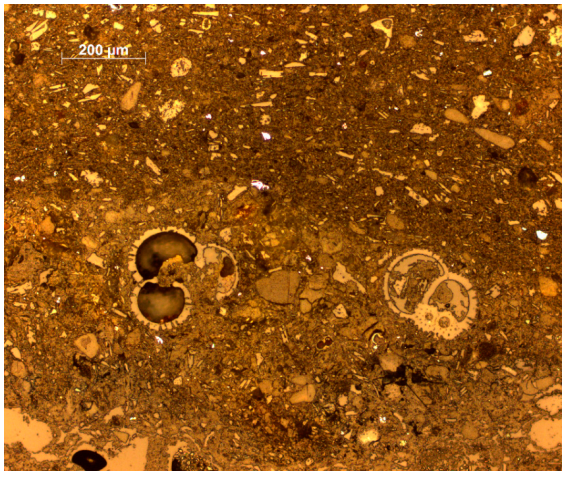

Plate C26. Reflected light image showing the dense nature of the matrix, some micro-fossils (foraminifera), and a slight change in matrix density between the upper part and the lower part of the image.

3.5.3. SEM Analysis

The BSEM images reveal the extent of the fracturing which is pervasive throughout the sample (Plate C27). In general, fracturing has propagated around the coarser grains: very few are themselves fractured. No evidence of secondary precipitation was observed. Some differences in porosity were observed: areas of finer grained material appear less porous than coarser areas. These differences in finer grained and coarser grained areas reflect the original sedimentary deposition textures (Plate C28).

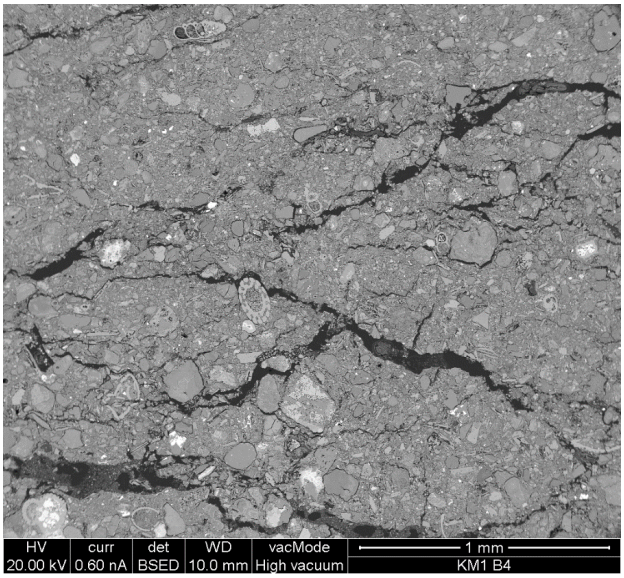

Plate C27. BSEM image showing the nature of the fracturing: very few of the larger grains are themselves fractured, the fractures have largely propagated around these coarser grains.

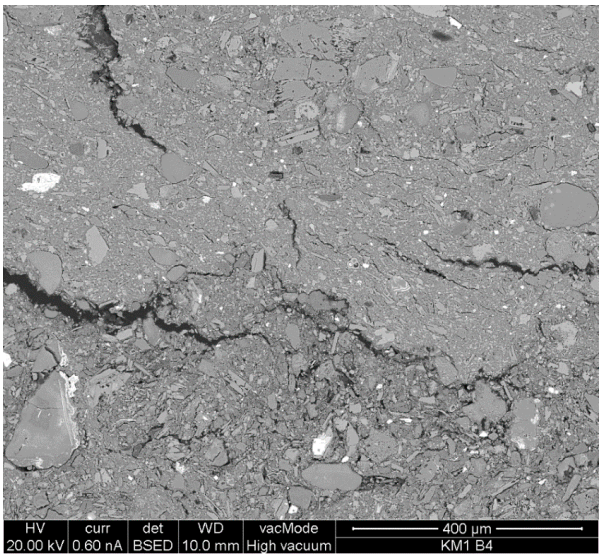

Plate C28. BSEM image showing some differences in texture: upper portion has a lower porosity than lower half of image, and is finer grained. This reflects differences in the original sediment deposition.

3.6. KM1 B5

3.6.1. Hand Sample

The sample was mid-brown, fine-grained and homogenous. The sample remained cohesive when broken apart, but the resulting surface texture was rough.

Plate C29. Photographs of the hand sample. **Left**: the sample prior to splitting; **Right**: half of the split sample showing the internal texture.

3.6.2. Optical Analysis

The sample is cross-cut throughout by sharp angular fractures (Plates C30 and C31). These are clean with no evidence of secondary precipitation. Fractures have propagated around coarser, more competent grains. The matrix is dense and contains micro-fossils. Bands of varying porosity were identified within the sample which reflect original sedimentary deposition features. These bands do not appear to have influenced the fracturing. However, some fractures have been influenced by thin, dense, horizontal seams, which have caused the fractures to jump en-echelon (Plate C32).

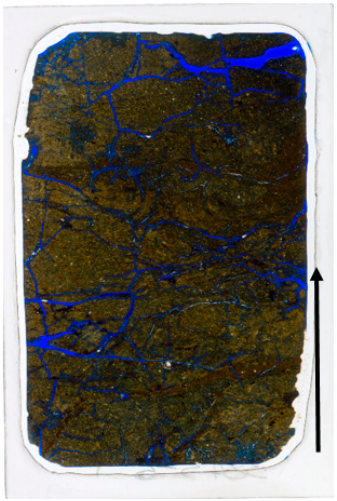

Plate C30. Scanned image of the thin section showing way-up orientation.

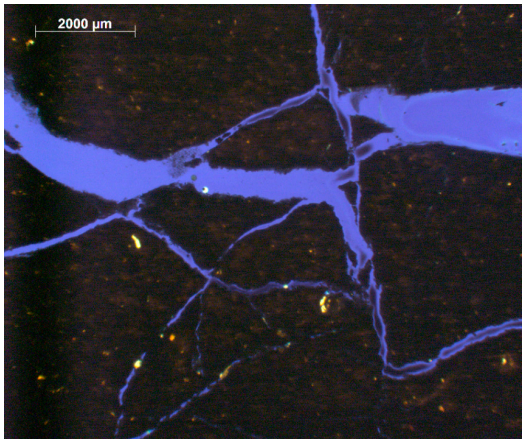

Plate C31. PPL image showing the angular nature of the fracturing.

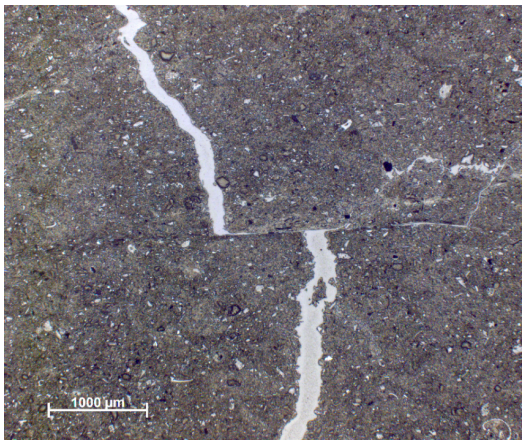

Plate C32. Reflected light image shows how a fracture has moved en-echelon along a thin, dense, horizontal seam.

3.6.3. SEM Analysis

BSEM imaging shows that some larger fractures have been lined with a fine-grained material which is richer in Mg than the host bentonite material (Plate C33), and which appears to be secondary. The matrix is dense and contains micro-fossils. There are bands of denser, more fine-grained material (<1.5 mm wide), which are related to original deposition features. These contain intense micro fracturing oriented parallel to the band (Plate C34).

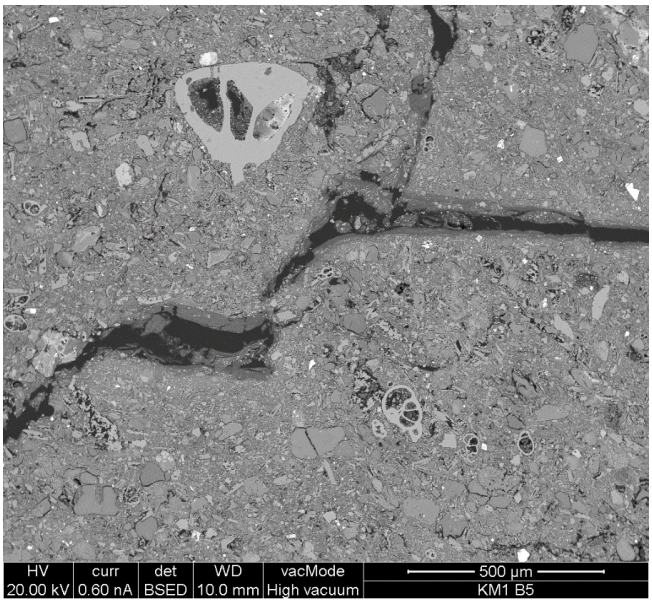

Plate C33. BSEM image showing more Mg-rich material lining the fracture (dark grey).

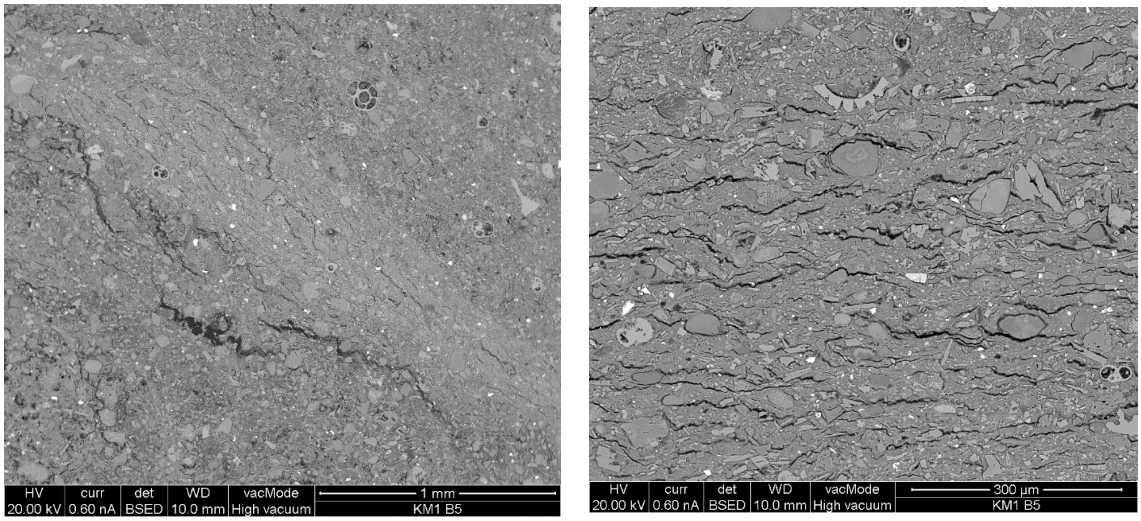

Plate C34. Left: BSEM image of one of the denser, finer-grained bands; **Right**: detail from the centre of the band showing the intense micro fracturing parallel to the orientation of the band.

3.7. KM1 B6

3.7.1. Hand Sample

The sample was mid-brown, fine-grained and homogenous. The sample remained reasonably cohesive when broken apart, but the resulting surface texture was rough.

Plate C35. Photographs of the hand sample. **Left**: the sample prior to splitting; **Right**: half of the cut sample showing the rough internal texture.

3.7.2. Optical Observations

The sample is fractured throughout. The larger fractures are pull-apart type fractures which displayed no evidence of secondary precipitation. However, micro fracturing is intense in some areas of the sample, and these fractures are more sinuous (Plate C37). Some of the larger fractures have been controlled to some extent by differences within the lithology (e.g., fractures have propagated along the boundaries between finer grained bands and coarser grained bands). However, there are also instances where the fractures have cut these lithological bands perpendicular to banding. Fractures have also propagated around pre-existing 'clots' of material which are most likely pelloids (Plate C38).

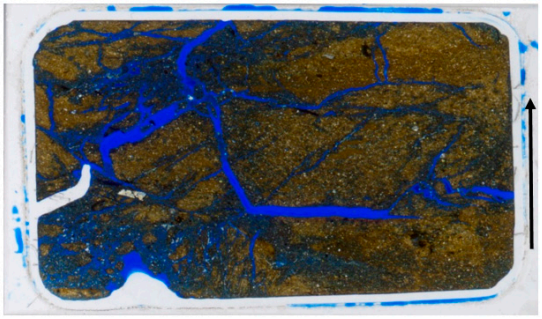

Plate C36. Scanned image of the thin section showing way-up orientation.

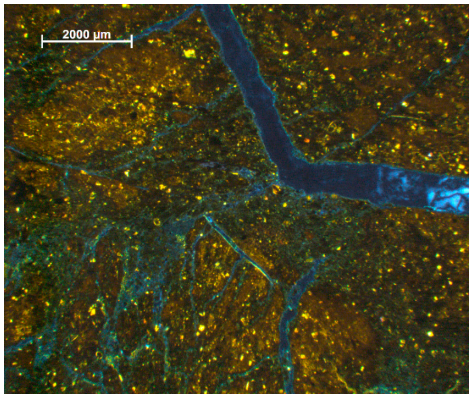

Plate C37. PPL image showing a major, angular pull-apart fracture, and an intense network of more sinuous micro fractures.

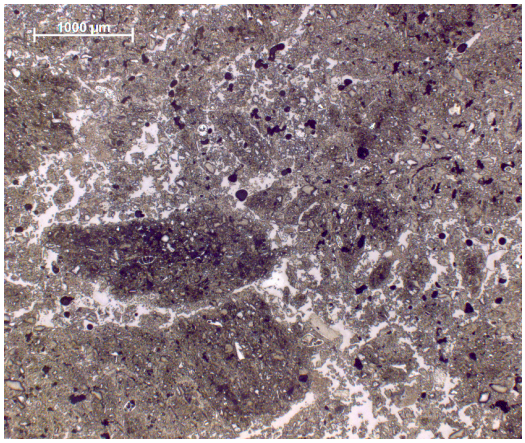

Plate C38. Fracturing has highlighted some pre-existing features within the lithology: in this case these 'clots' are probably pelloids.

3.7.3. SEM Analysis

Under the SEM, it is apparent that the entire sample is pervasively fractured. Larger fractures are pull-apart fractures, and have no secondary mineralisation except for some Fe present within some fractures (Plate C39). Generally the larger fractures form a cross cutting network of conjugate faults, although some curved listric faulting is present (Plate C39). Areas which appear homogenous in hand sample/optical are intensely micro fractured (Plate C40). There is an increase in porosity along some fracture margins.

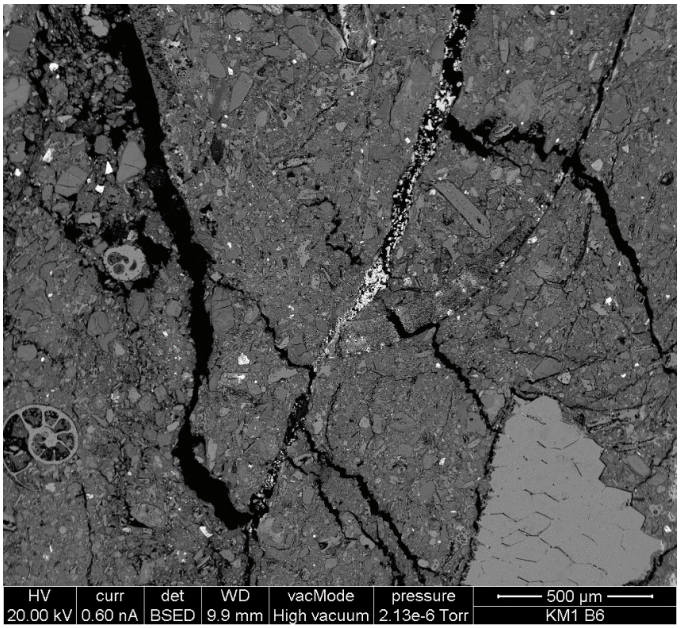

Plate C39. BSEM image of some of the major faults within the sample. Most here form a network of straight conjugate faults, but a curved listric fault crosses the centre of the image. Some Fe mineralisation is present within some faults.

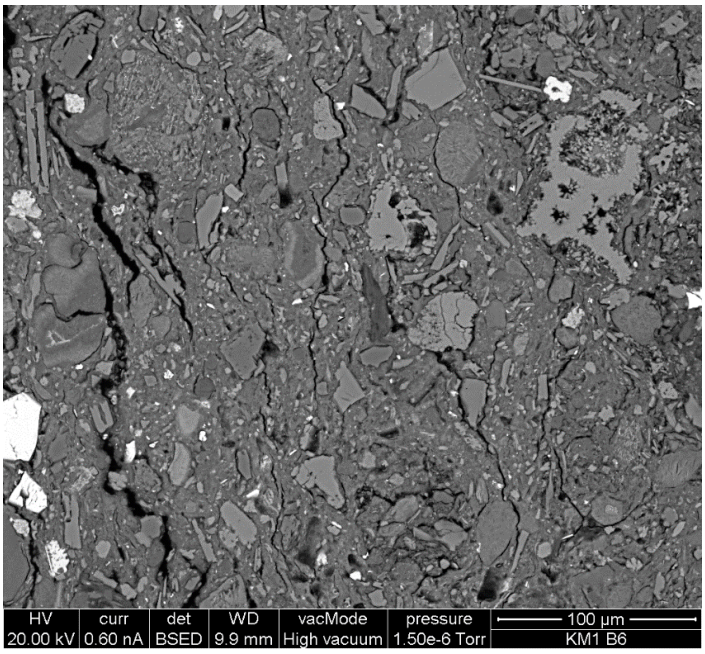

Plate C40. Detail of the pervasive micro fracturing within the sample. Micro fractures have propagated around more competent grains.

3.8. KM1 B7

3.8.1. Hand Sample

The sample is mid-brown, homogenous in appearance but was relatively crumbly when split. Fractures were apparent throughout the sample prior to splitting.

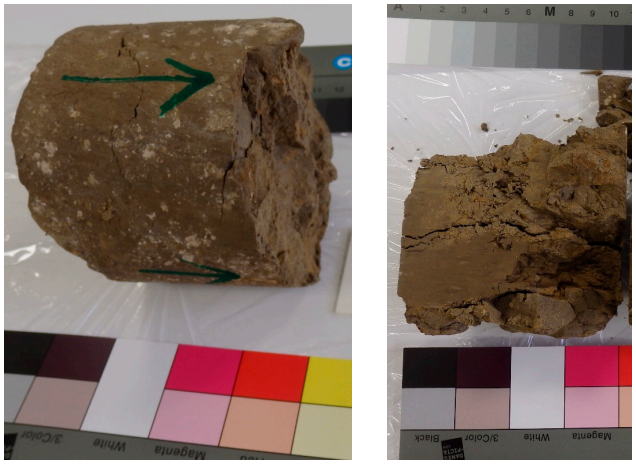

Plate C41. Photographs of the hand sample. **Left**: the sample prior to splitting; **Right**: half of the split sample showing the internal texture.

3.8.2. Optical Analysis

The matrix is dense and fossiliferous. There is a network of fractures across the sample dominated by horizontal/sub-horizontal fractures. Some bands within the section are highly porous. Pre-existing bedding features have influenced the fracturing to some extent e.g., propagation along very fine grained seams, or fracturing around more dense 'clots'—palletisation.

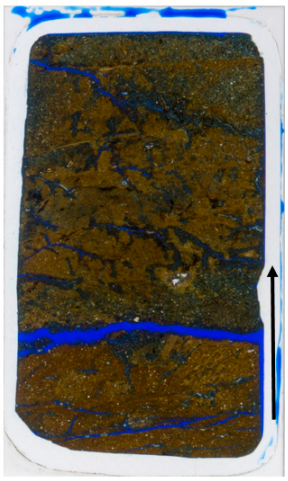

Plate C42. Scanned image of the thin section showing way-up orientation.

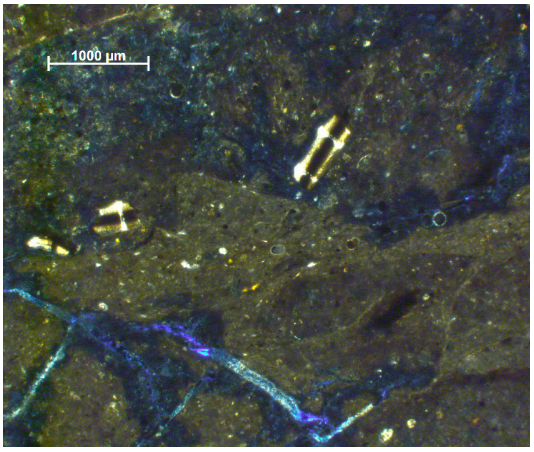

Plate C43. PPL image showing contrast between areas of lower porosity (bottom) and higher porosity (top). Propagation of fractures have been controlled to some extent by bedding features.

3.8.3. SEM Analysis

Imaging revealed intense micro fracturing throughout the sample. The dominant orientation of the micro fractures changes markedly from sub-horizontal to sub-vertical within differing areas of the section (Plate C44). There is minor pelletisation of the sample in some areas, where micro fractures have propagated around packets of bentonite with differing grain size or density. No evidence for secondary precipitation other than some minor Fe mobilisation.

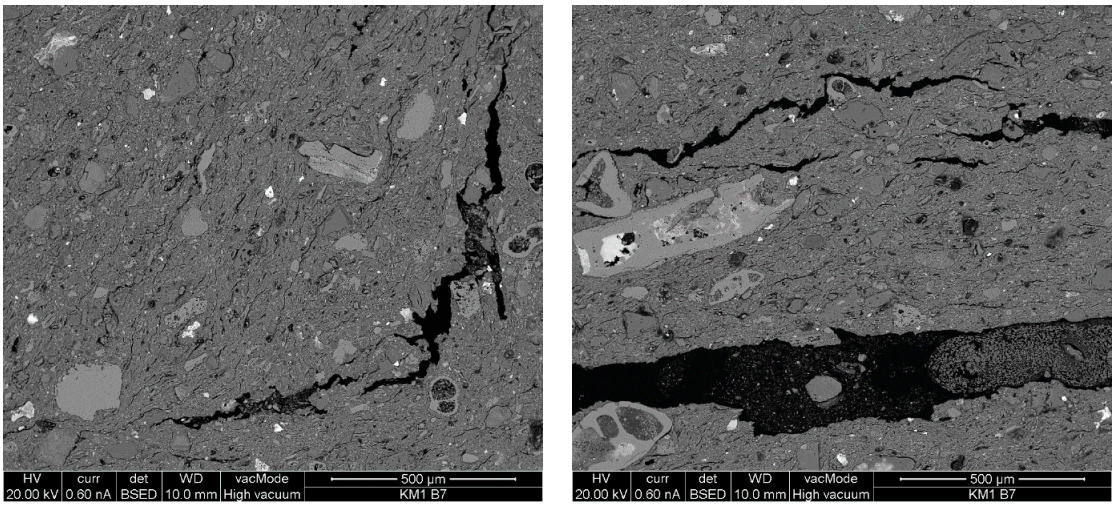

Plate C44. BSEM images showing the change in fracture orientation between two areas of the sample. **Left**: micro fracturing is sub-vertical; **Right**: micro fracturing is sub-horizontal.

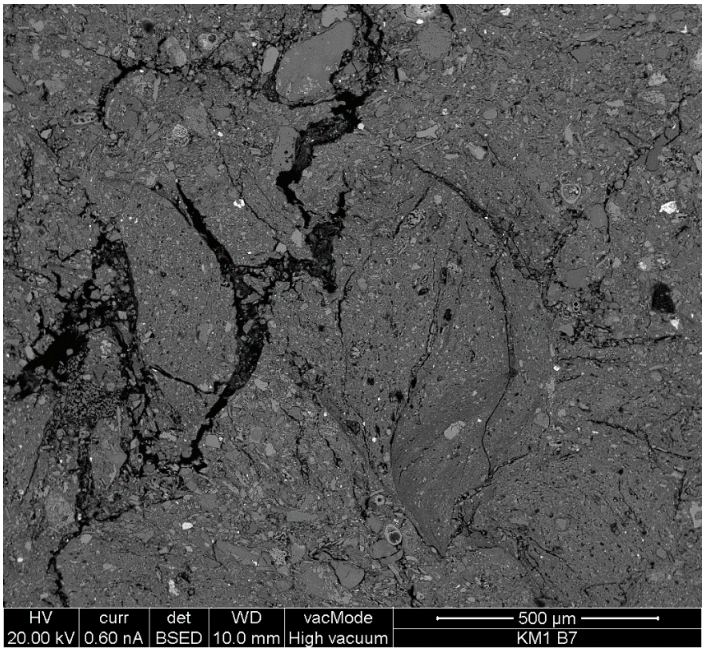

Plate C45. BSE image showing pelletisation by micro fractures propagating around areas of differing grain size and/or density.

3.9. KM2 B3

3.9.1. Hand Sample

Dense, soft, fine grained bentonite sample. The sample was not marked with a way-up orientation. When split, the internal structure of the sample showed a curved structure throughout (also apparent on the thin section). This may be due to an artefact of the core drilling, either dragging the edges of the sample up or down.

Plate C46. Photographs of the hand sample. **Left**: the sample prior to cutting; **Right**: half of the cut sample showing the internal texture.

3.9.2. Optical Observations

The matrix is fine-grained with occasional coarser clasts (<150 μm). However, porosity is widespread throughout the section as evidenced by the blue dye. No evidence was observed for secondary precipitation within the fractures.

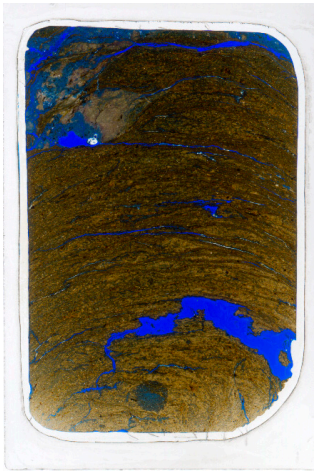

Plate C47. Scanned image of the thin section. No way-up orientation was provided for this sample.

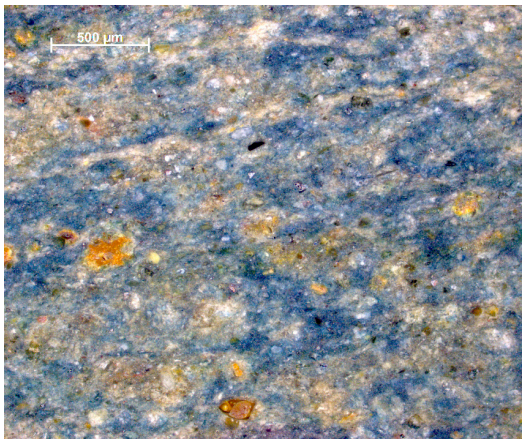

Plate C48. Darkfield image from central area of section showing extent of porosity (blue areas). The porosity has a sub-horizontal orientation.

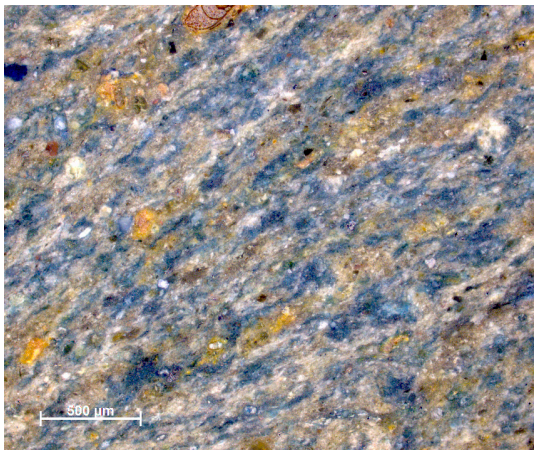

Plate C49. Darkfield image from edge of section showing extent of porosity (blue areas). The porosity has an oblique orientation (contrast to Plate C49).

3.9.3. SEM Analysis

The top left corner of the section has a lighter area (see scan of thin section, Plate C47). EDXA analysis indicated that this is an area of carbonation. The carbonation is diagenetic, but not related to fracturing processes. Micro fractures are pervasive throughout the sample. No secondary precipitation is present.

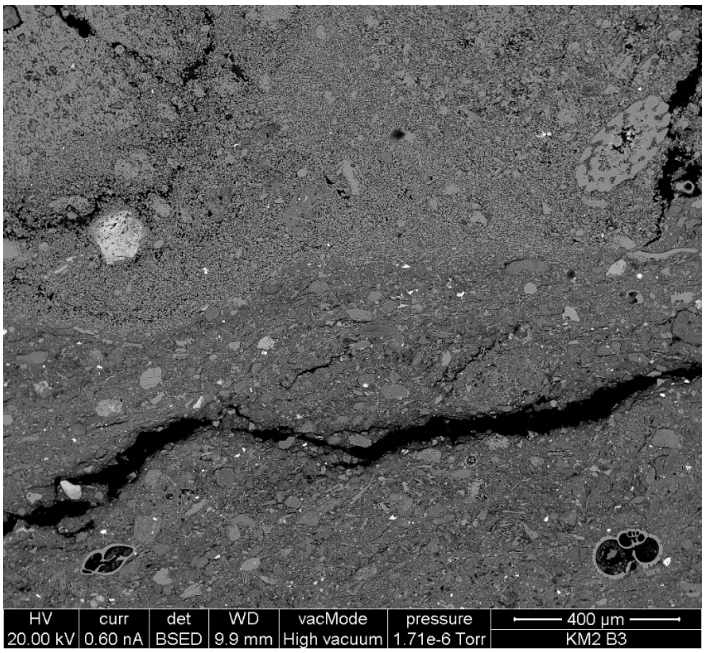

Plate C50. BSE image showing carbonated area (top). This area is sharply delineated from the non-carbonated matrix below.

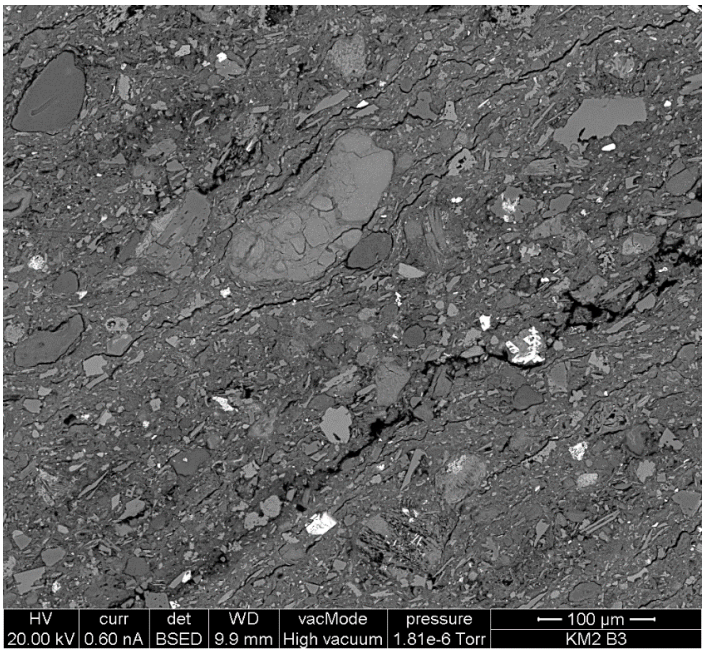

Plate C51. BSEM image detailing the micro fracturing within the matrix. The fracturing has propagated around the more competent grains.

3.10. KM2 B4

3.10.1. Hand Sample

This is a light brown, fine-grained sample which split smoothly. Variation in colour within sub-horizontal bedding, ranging from pale cream to light brown was apparent across the split sample.

Plate C52. Photographs of the hand sample. **Left**: the sample prior to cutting; **Right**: half of the cut sample showing the internal texture.

3.10.2. Optical Observations

Matrix is rich in micro fossils (Plate C54). The thin section shows three distinct, evenly distributed, sub-horizontal banding comprising of a finer-grained matrix which is denser and lower in porosity (Plate C55). Many of the micro-fractures have an en-echelon texture. No evidence for secondary precipitation is present.

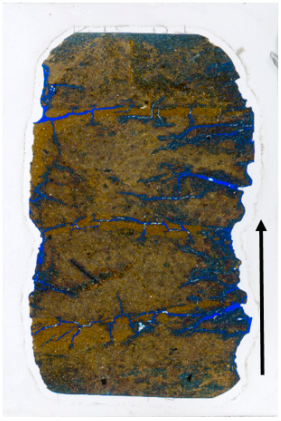

Plate C53. Scanned image of the thin section showing way-up orientation.

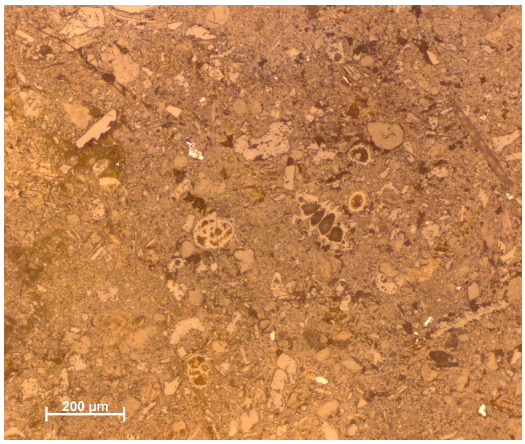

Plate C54. Reflected light image showing the fossiliferous nature of the matrix.

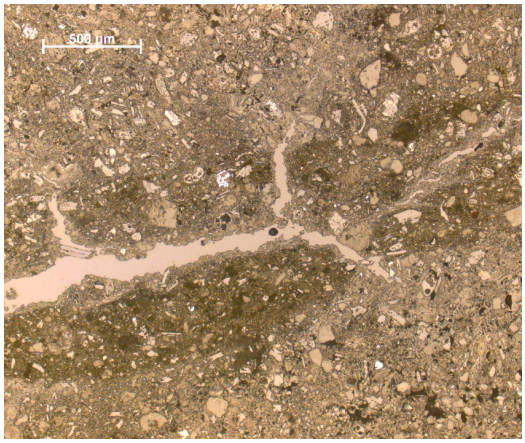

Plate C55. Reflected light image showing one of the denser, sub-horizontal bands. The material on either side of the band has a higher porosity. A fracture is present in the centre of the denser band.

3.10.3 SEM Analysis

BSEM imaging highlighted the contrast between the dense bands and the more porous matrix. The dense bands are finer grained as shown by Plate C56. The matrix is fossil rich, containing both fossil fragments and micro-fossils. The matrix is extensively micro fractured, with the micro fractures propagating around the coarser, more competent grains.

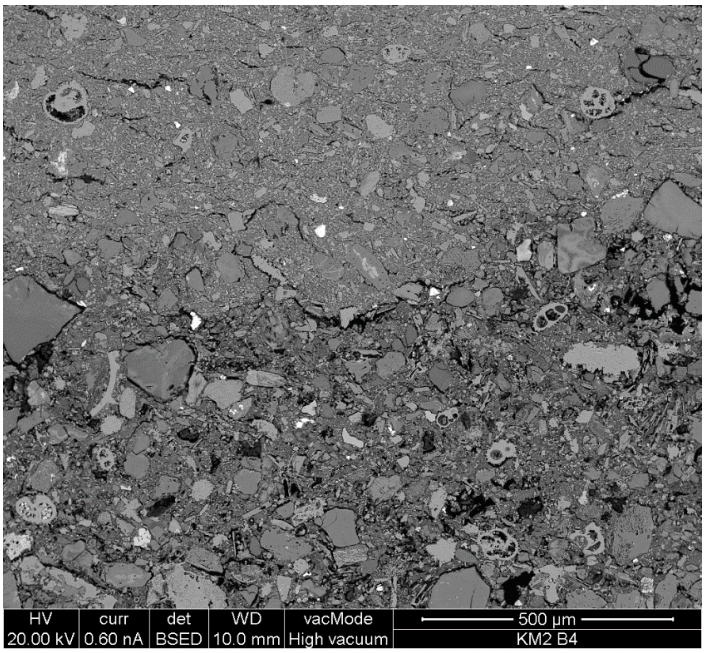

Plate C56. BSEM image showing the contrast between one of the dense, finer-grained, sub-horizontal bands (**top**) and the more porous matrix below.

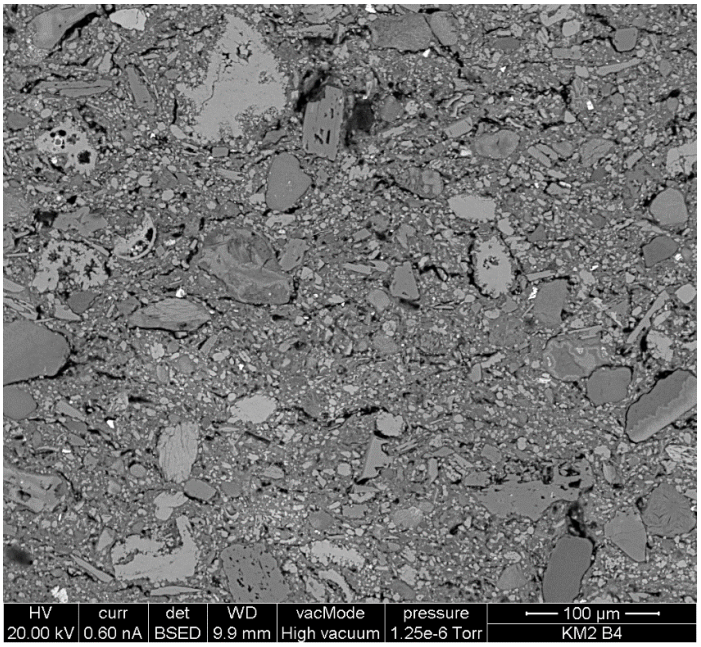

Plate C57. BSEM image of more porous matrix showing the pervasive micro fracturing. Fracturing has propagated around more competent grains.

3.11. KM2 B5

3.11.1. Hand Sample

The sample is a mid-brown, fine-grained bentonite with light cream veining and nodules, which are most apparent in the split sample. The split sample remained cohesive, but developed a rough texture following splitting, indicating numerous fractures.

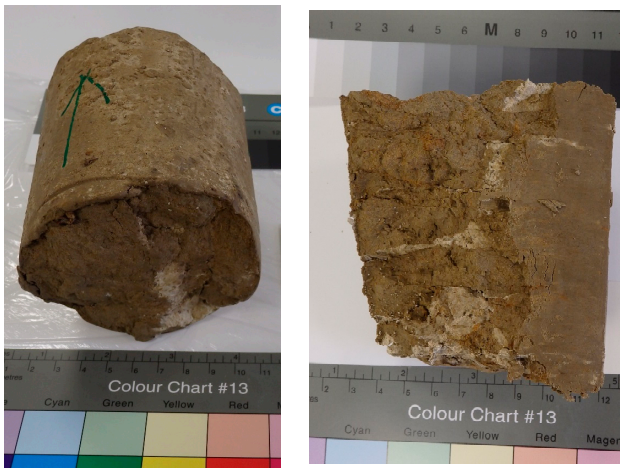

Plate C58. Photographs of the hand sample. **Left**: the sample prior to splitting; **Right**: half of the split sample showing the internal texture.

3.11.2. Optical Observations

The matrix is fine-grained which contrasts to the carbonated veins which have a granular texture, and comprise individual carbonate crystals (<30 μm). The carbonated veins are highly porous. The sample is fractured, with major fractures being associated with, or appearing within, the carbonated veins. Fractures are sinuous rather than highly angular.

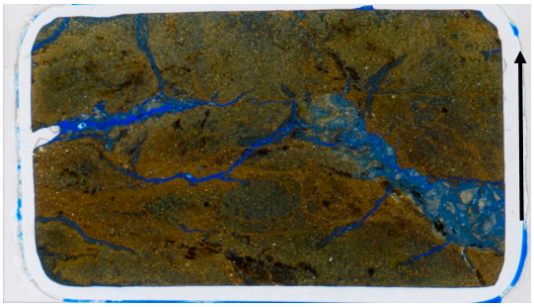

Plate C59. Scanned image of the thin section showing way-up orientation.

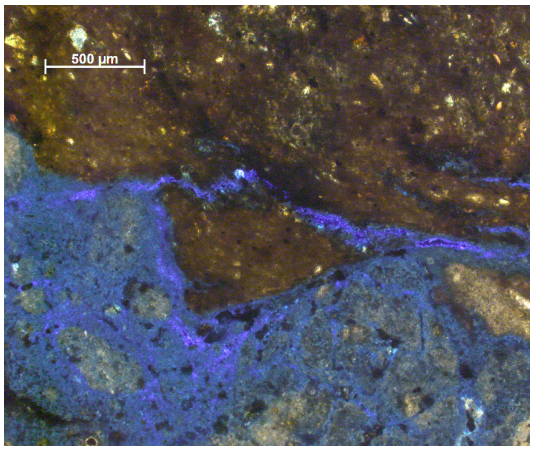

Plate C60. PPL image showing a porous, carbonate vein (bottom) and fine-grained, dense matrix above.

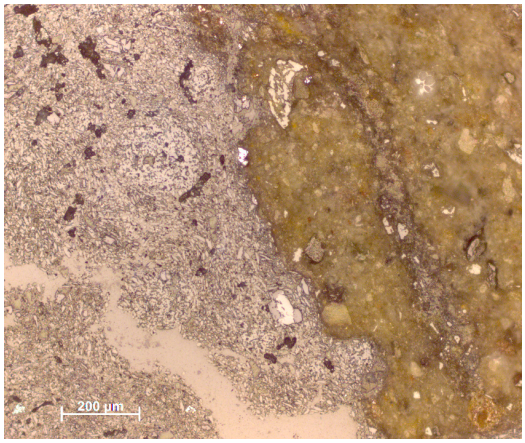

Plate C61. Reflected light image showing detail of the boundary between a granular, carbonated vein and the fine-grained bentonite matrix.

3.11.3. SEM Analysis

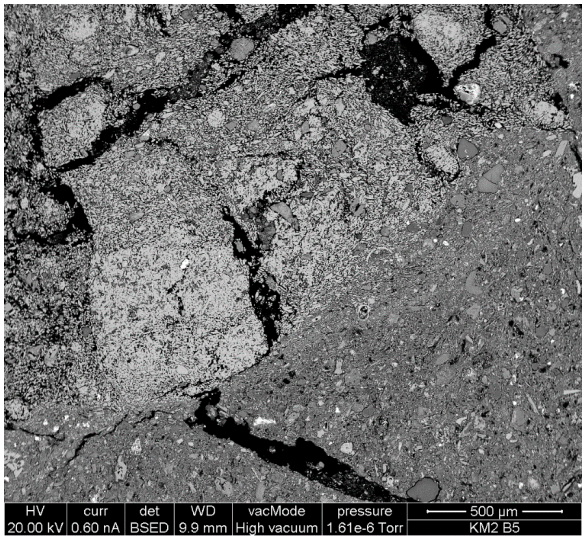

Plate C62. BSEM image showing a carbonated area (top) and non-carbonated bentonite matrix.

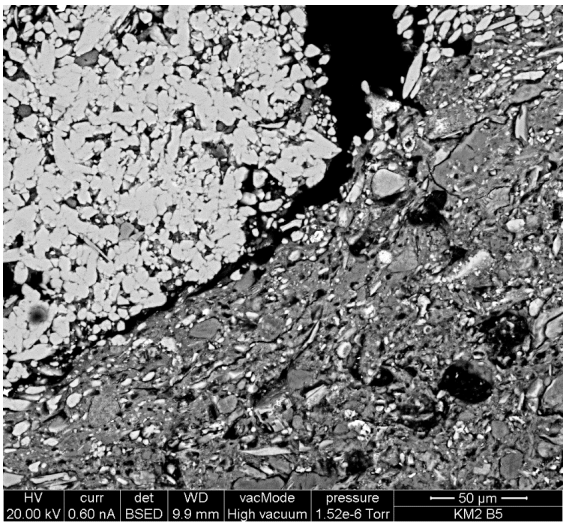

Plate C63. BSEM image showing detail of the granular carbonate and the contrast to the non-carbonated bentonite. A fracture has propagated at the boundary between the two.

3.12. KM2 B6

3.12.1. Hand Sample

A light brown, fine-grained bentonite clay which is homogenous. The sample appears less fractured in hand sample than many of the other samples, although some horizontal fractures are present.

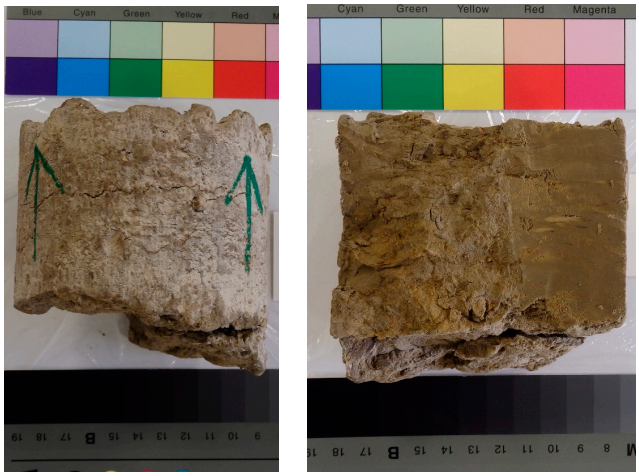

Plate C64. Photographs of the hand sample. **Left**: the sample prior to cutting; **Right**: half of the cut sample showing the internal texture.

3.12.2. Optical Observations

This sample has distinct bands of bedding which differ in porosity: highly porous bands alternate with less porous bands. This is clearly seen in the thin section scan (Plate C65). Fractures are broader and more angular within the less porous banding (Plate C66), and in these bands, the fractures are often cross-cutting, until meeting the more porous material where they become more sinuous and sub-horizontal. Fracture have also propagated at the boundaries of the change in lithology (Plate C67).

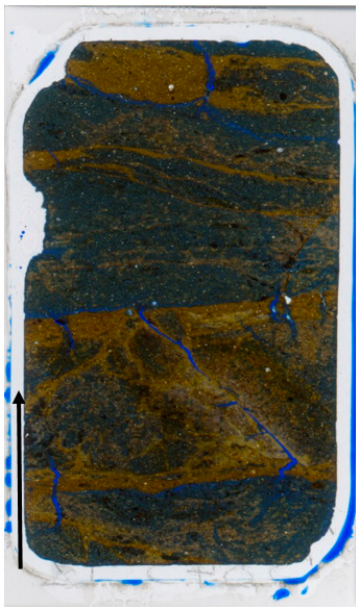

Plate C65. Scanned image of the thin section showing way-up orientation.

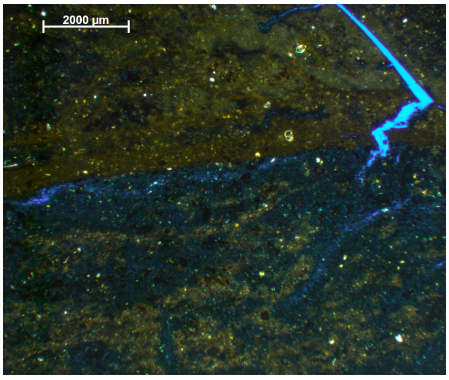

Plate C66. PPL image showing contrast between denser, less porous band (top) and more porous material (bottom). The nature of the fractures within the two lithologies is clearly illustrated.

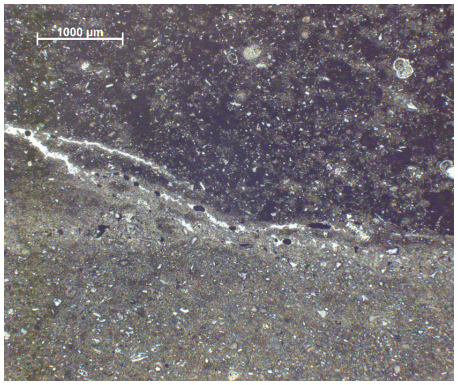

Plate C67. Reflected light image showing detail of a less porous band (top) and more porous material (bottom), with a micro fracture propagating at the boundary between them.

3.12.3. SEM Analysis

The difference in texture between the porous and less porous bands is marked (Plate C68), with the more porous bands comprising coarser material. Fractures in the less porous material are clean, pull-apart fractures with no evidence of secondary precipitation (Plates C68 and C69). In the more porous material, fractures are more sinuous, and partially infilled with debris, and micro fractures are extensive.

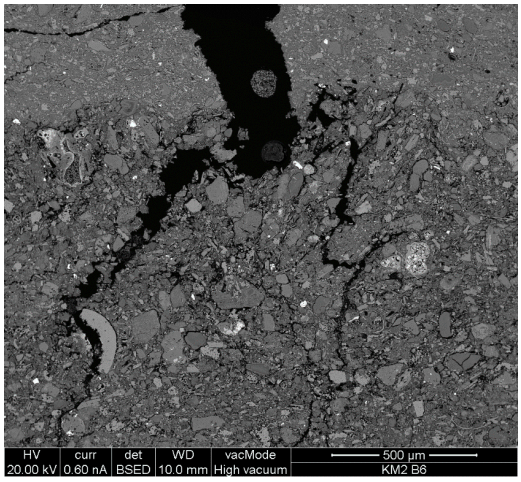

Plate C68. BSEM image showing the contract between a dense, low-porosity band (top) with clean, pull-apart fractures, and the high porosity band below. The fractures in the high porosity band are more sinuous and contain some debris material. Micro fractures are extensive within this band.

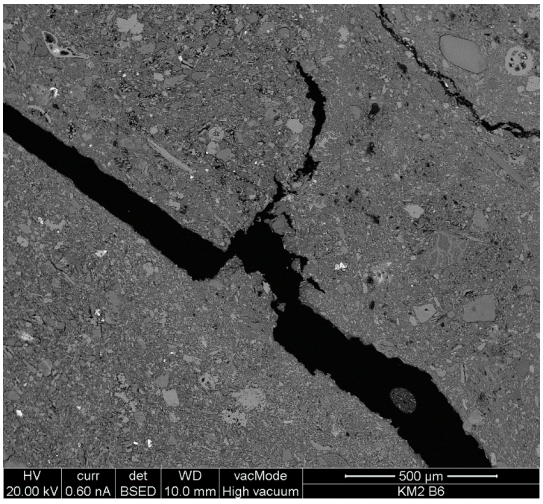

Plate C69. BSEM image of a near-perfect pull-apart fracture within a low porosity band.

3.13. KM2 B7

3.13.1. Hand Sample

This sample is light brown, fine-grained and split smoothly. There are some lighter, cream coloured areas visible in the interior of the core following splitting. These areas comprise both nodules and veining.

Plate C70. Photographs of the hand sample. **Left**: the sample prior to cutting; **Right**: half of the cut sample showing the internal texture.

3.13.2. Optical Observations

The matrix is fine grained with a high degree of porosity throughout. There are some sinuous bands of matrix which are finer grained with a lower porosity. Carbonate nodules towards the bottom of the section are also of variable porosity, with the most densely carbonated areas having the lowest porosity. Major fractures within the matrix are clean, pull-apart fractures. These are abruptly terminated when encountering a carbonated area: the fractures become micro-scaled and sinuous, reverting to a clean cut major fracture on the opposite side of the carbonated area (Plate C72).

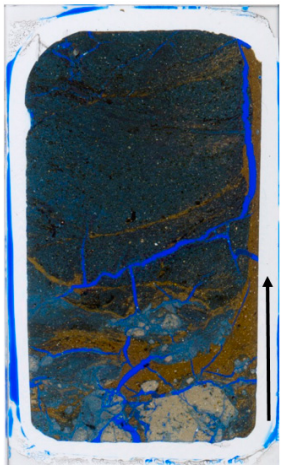

Plate C71. Scanned image of the thin section showing way-up orientation.

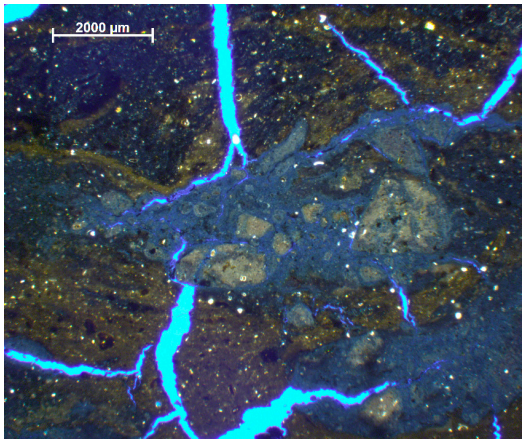

Plate C72. PPL image showing the nature of the major fractures when encountering a carbonated area (Centre).

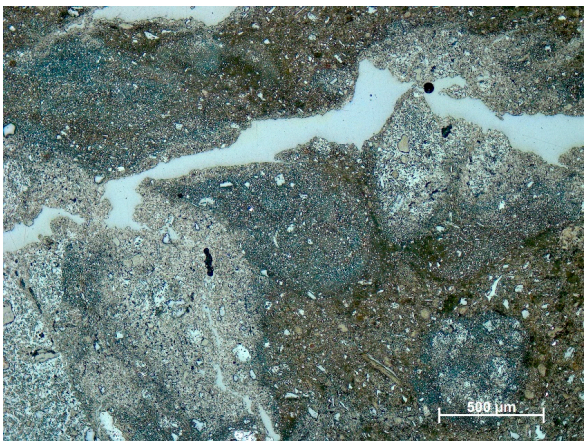

Plate C73. Reflected light image highlighting differences in the nature of the sample. This image shows pellets of bentonite which have varying porosity. The pellets are cross-cut by a major fracture.

3.13.3. SEM Analysis

EDXA confirmed the presence of calcium carbonate, and BSEM images clearly show the carbonated areas (Plate C74). Where carbonation is most intense, nodules have formed, around which micro fractures have propagated. The contrast between the bentonite matrix and the carbonated material is marked (Plate C75).

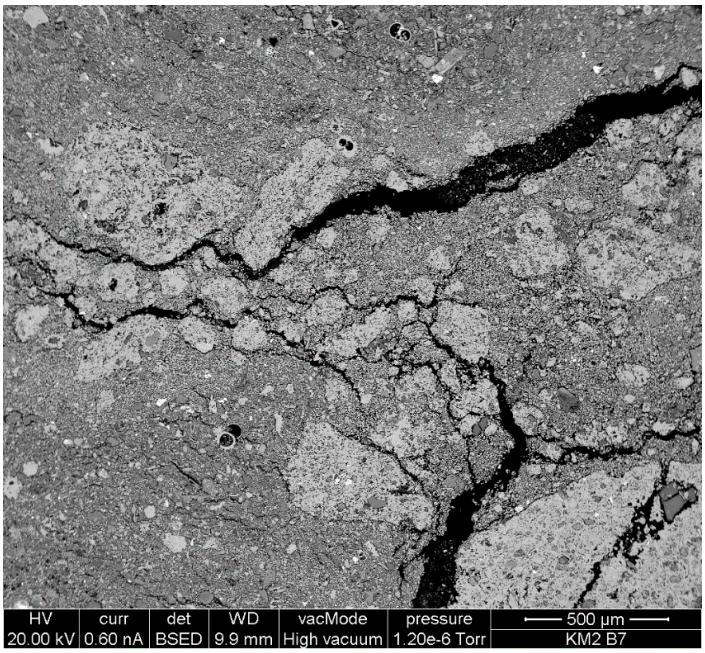

Plate C74. BSEM image showing a carbonate area with several carbonated nodules. Micro fracturing is extensive within the carbonated area.

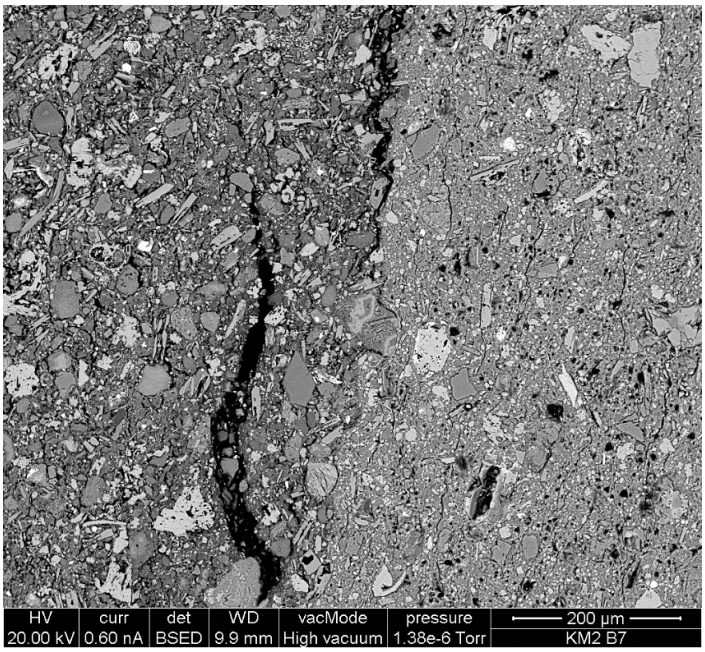

Plate C75. BSEM image showing detail of, and contrast in the matrix. The coarser, higher porosity area on the left contains less carbonate than the finer-grained, lower porosity area on the right. However, very fine micro fractures are extensive throughout both lithologies.

3.14. KM3 B1

3.14.1. Hand Sample

Light brown, homogenous sample. Highly fractured: on splitting, the sample largely crumbled into equant pieces. The pattern of equant fracturing is also present in the more cohesive fractions of the sample.

Plate C76. Photographs of the hand sample. **Left**: the sample prior to splitting; **Right**: half of the split sample showing the internal texture.

3.14.2. Optical Observations

The sample appears pulverised with a network of angular fractures. There is no overriding preferential direction of fracturing. Fossils are rare; the sample is extremely fine-grained.

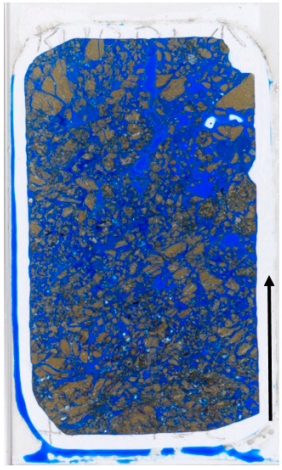

Plate C77. Scanned image of the thin section showing way-up orientation.

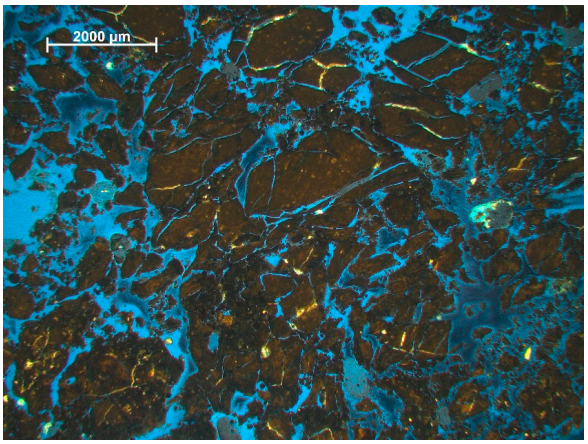

Plate C78. PPL image showing the pulverised nature of the sample. The fractures are dominantly angular.

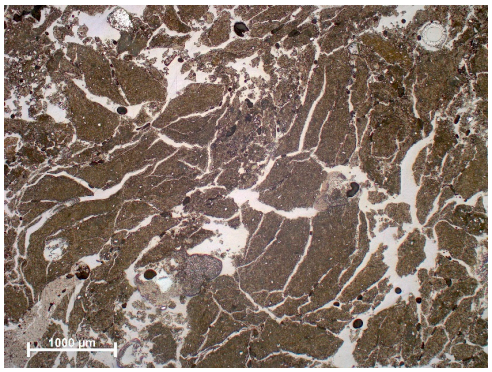

Plate C79. Reflected light image showing the extensive nature of the fracturing and the homogenous, fine-grained nature of the bentonite.

3.14.3. SEM Analysis

BSEM imaging highlights the homogenous and fine-grained nature of the bentonite (Plate C80). Fracturing is extensive and the sample has been pulverised into reasonably equant pieces (Plate C81). Micro fracturing is present within these pieces (Plate C80).

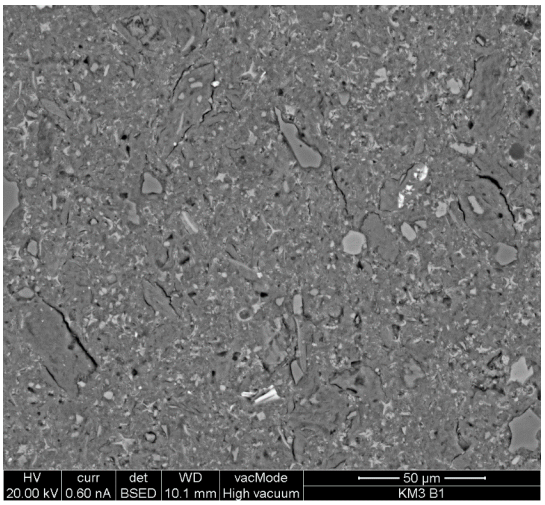

Plate C80. BSEM image showing detail of the matrix. This is fine grained and contains only rare micro fossils. There is some minor micro fracturing.

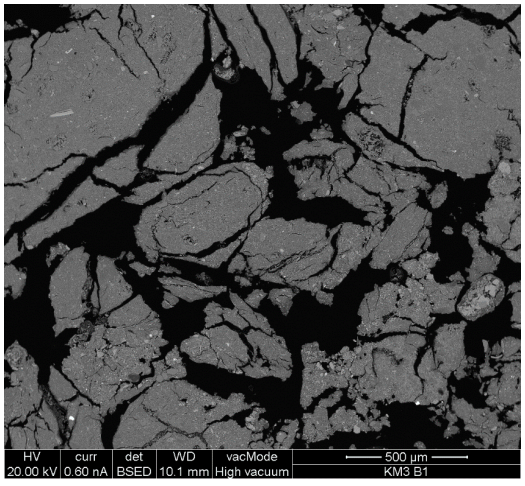

Plate C81. BSEM image showing the extensive fracturing.

3.15. KM3 B2

3.15.1. Hand Sample

This sample was a thin disc with no way-up orientation marked. The sample was a light brown colour, fine grained and homogenous in appearance.

Plate C82. Photograph of the hand sample prior to thin sectioning.

3.15.2. Optical Observations

Sample is highly fractured. Sample has a "pelleted" texture (clearly illustrated under reflected light).

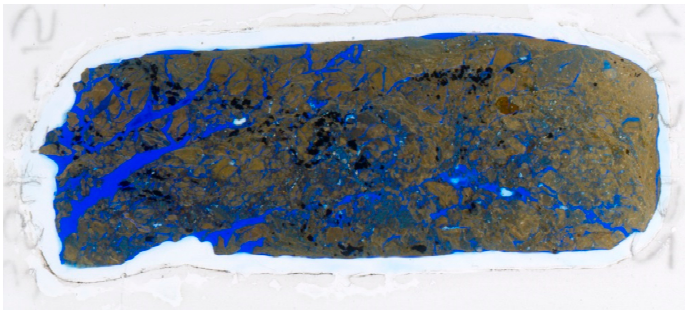

Plate C83. Scanned image of the thin section. No way-up orientation was provided for this sample.

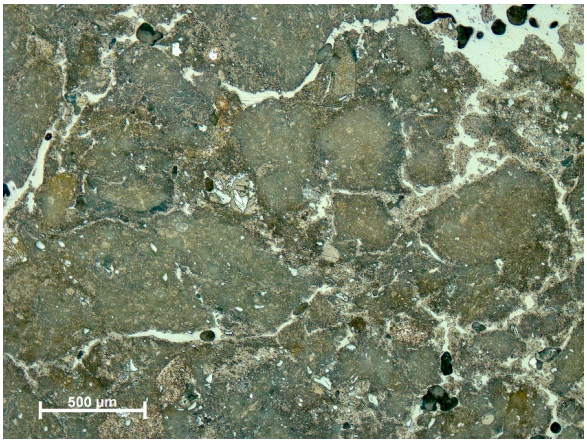

Plate C84. Reflected light view showing 'pelleted' texture formed by slight textural differences within the bentonite and fracturing.

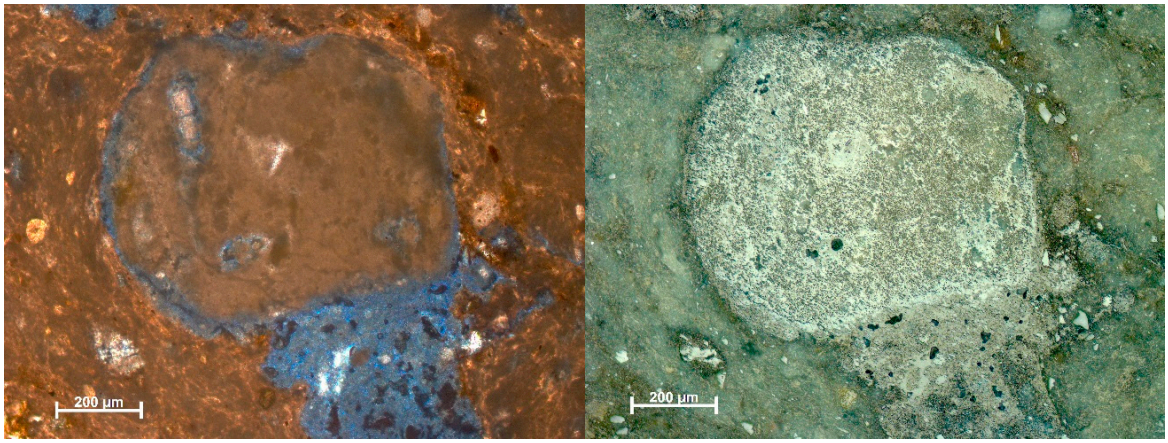

Plate C85. Example of a 'pellet'. **Left**: PPL image showing a pellet with a finer-grained texture than the surrounding material. This has been highlighted by fracturing around the boundaries of the pellet; **Right**: reflected light image which clearly highlights the different textures and composition between the pellet and surrounding matrix.

3.15.3. SEM Analysis

BSEM and EDXA spectra revealed dendritic Mn-rich mineralisation (Plate C86) and areas of carbonation and calcium carbonate nodules (Plate C87). The Mn mineralisation is secondary and pre-dates the fracturing, as does the carbonation which is diagenetic. The sample is extensively fractured, and the fine-grained matrix contains numerous micro fractures.

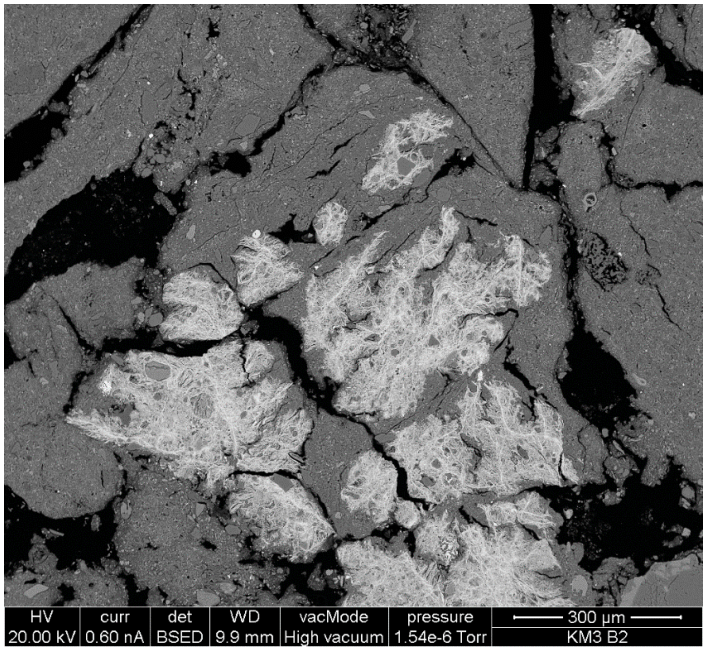

Plate C86. Mn mineralisation. This dendritic mineralisation pre-dates the fracturing.

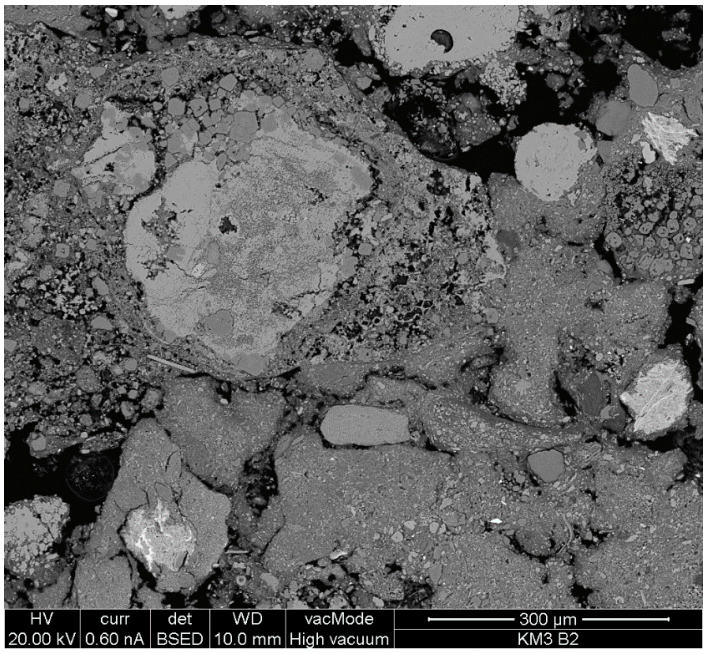

Plate C87. Detail of carbonation and carbonate nodules within the sample.

3.16. KM3 B3

3.16.1. Hand Sample

A very pale, fine-grained, homogenous sample. This sample contains numerous fractures: larger oblique fractures on the outer surface of the core, and on the internal split surface, a network of finer extensive fractures, giving an equant texture. The sample remained cohesive following splitting.

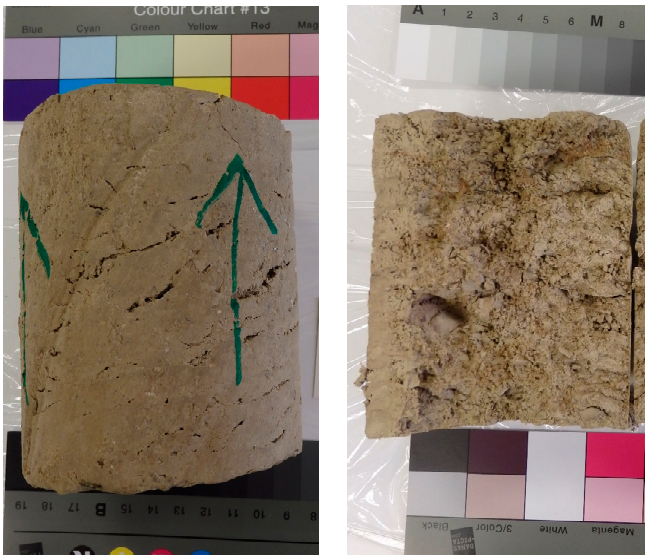

Plate C88. Photographs of the hand sample. **Left**: the sample prior to cutting; **Right**: half of the cut sample showing the internal texture.

3.16.2. Optical Observations

The fracturing within the sample is extreme; this is clearly illustrated in the scan of the thin section (Plate C89). There are distinctly different clasts within this sample: a coarse carbonate nodule (<6 mm) midway down the section (Plate C90), and opaque clasts (<2 mm) towards the top to the thin section (Plate C91). The bentonite matrix is fine-grained and homogenous.

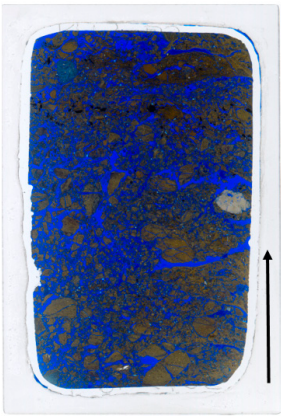

Plate C89. Scanned image of the thin section showing way-up orientation.

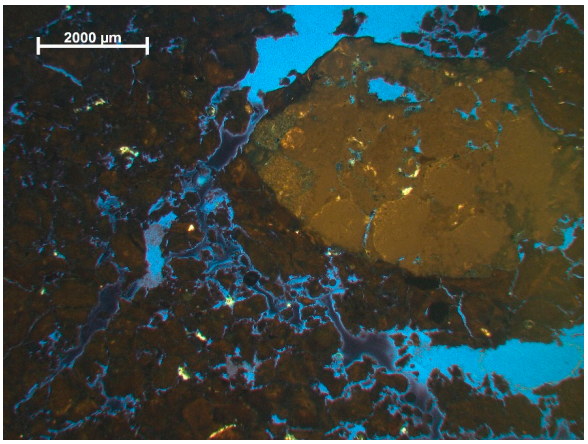

Plate C90. PPL image showing a carbonate nodule within the highly fractured bentonite.

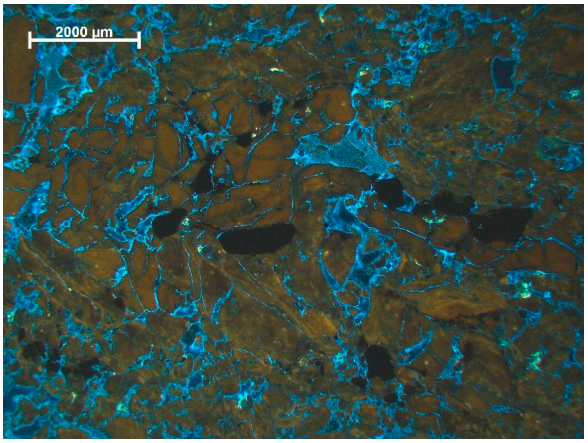

Plate C91. PPL image showing opaque material within the highly fractured bentonite.

3.16.3. SEM Analysis

BSEM and EDXA analysis show that as well as the large carbonate nodule there are some finer carbonate nodules (<500 µm), which have also been partially mineralised with Mn-rich mineralisation. The opaque nodules comprise dendritic Mn-mineralisation (Plates C92 and C93). Fracturing has been partially controlled by the mineralisation with some fractures propagating along the boundary of the carbonation or mineralisation. In the case of the Mn-mineralisation, the fractures have tended to propagate along where the mineralisation is most concentrated. The bentonite is fine grained and highly fractured. Micro fracturing is extensive within the still competent clasts of bentonite.

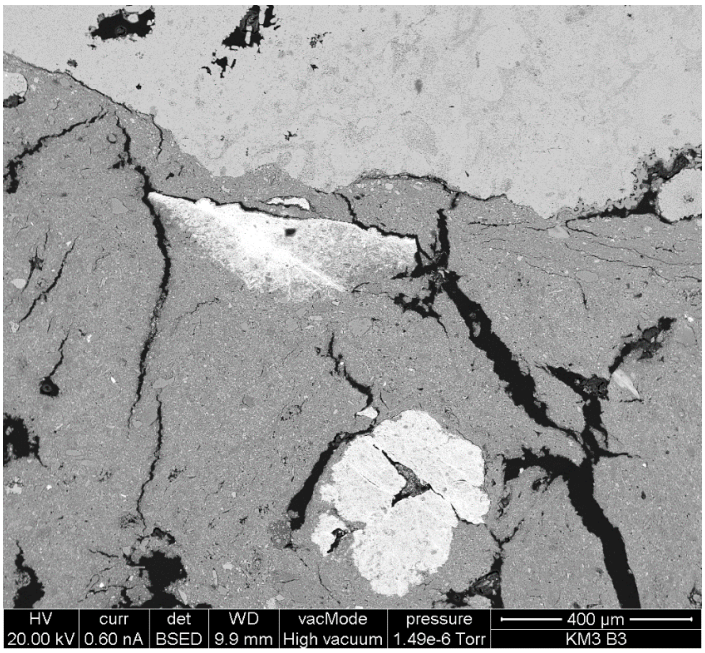

Plate C92. BSEM image showing the edge of a carbonate nodule (top), dendritiec Mn-rich mineralisation (bright white, centre), and a smaller carbonate nodule (bottom) which also contains some Mn mineralisation.

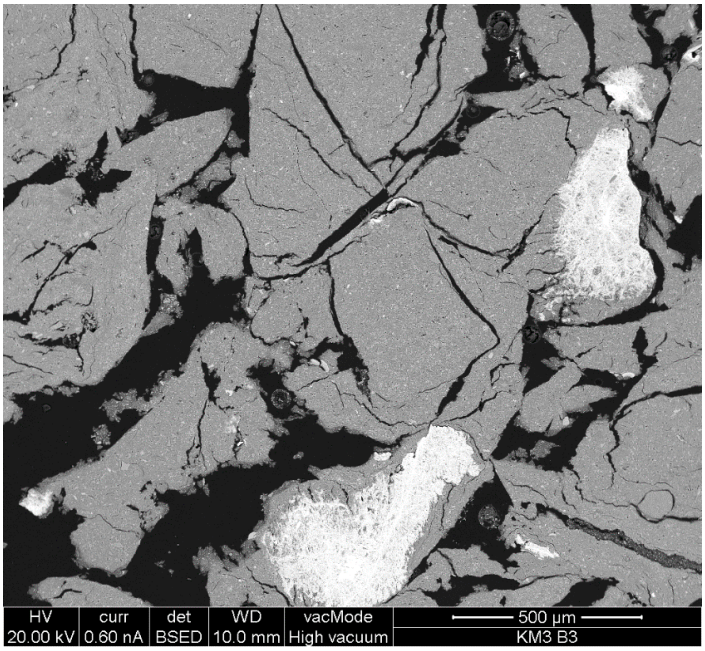

Plate C93. BSEM image showing highly fractured, fine grained bentonite and Mn-rich, dendritic mineralisation.

3.17. KM3 B4

3.17.1. Hand Sample

A dark reddish-brown, fine grained bentonite. This split fairly evenly and remained competant, but the resulting internal surface was reasonably rough, indicating numerous fractures are present.

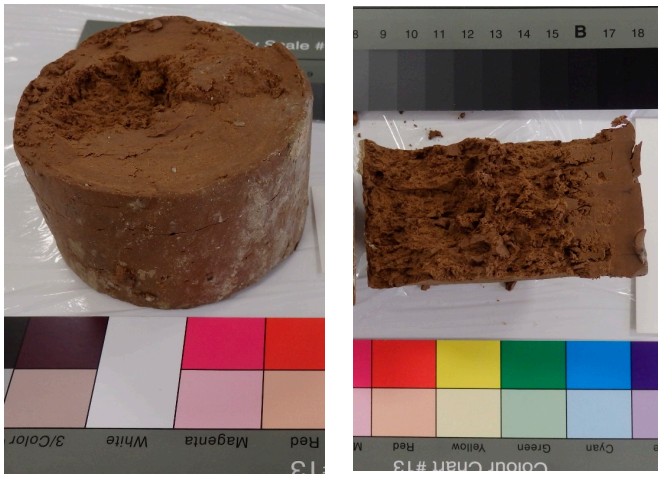

Plate C94. Photographs of the hand sample. **Left**: the sample prior to cutting; **Right**: half of the cut sample showing the internal texture.

3.17.2. Optical Observations

The bentonite is very fine-grained with very rare microfossils. Plate C95 indicates fractured, but reasonably competent material on the left side of the thin section, whilst the right side of the section is extensively fractured. Optical imaging of areas on the left side show an anastomosing network of fine, lighter coloured material which is probably a result of shear and strain (Plate C96). A pelleted or 'chicken wire' texture is developing where rounded clasts of more competent, less strained material is encompassed by this network of fine, lighter coloured shear pathways. Porosity and fracturing is starting to develop alone this network (Plate C97). On the right side of the thin section where fracturing is more extensive, the material has been broken down into individual clasts of bentonite. Only a limited amount of evidence of the fine, shear network remains where fracturing and porosity has not been fully developed.

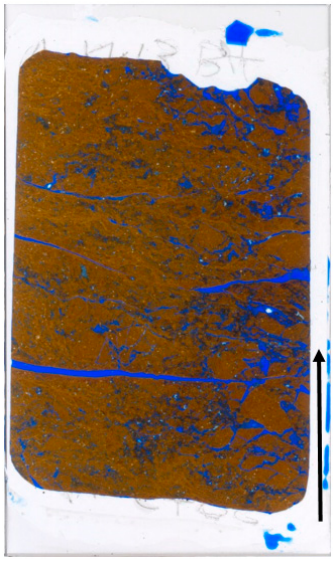

Plate C95. Scanned image of the thin section showing way-up orientation.

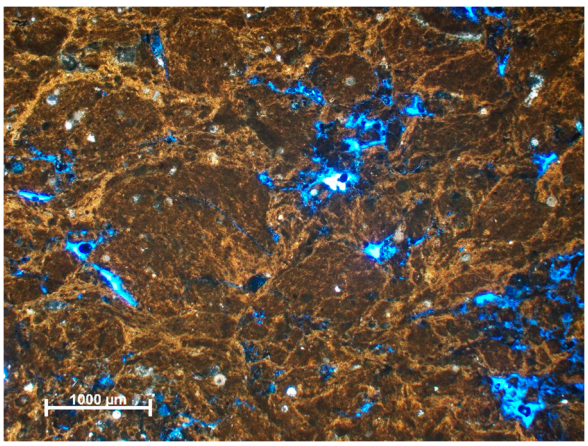

Plate C96. PPL image of the more competent material on the right side of the thin section. A 'chicken-wire' texture is developing with clasts of competent material defined by an anastomosing network of fine, lighter coloured material. Porosity and fracturing is beginning to develop along this network.

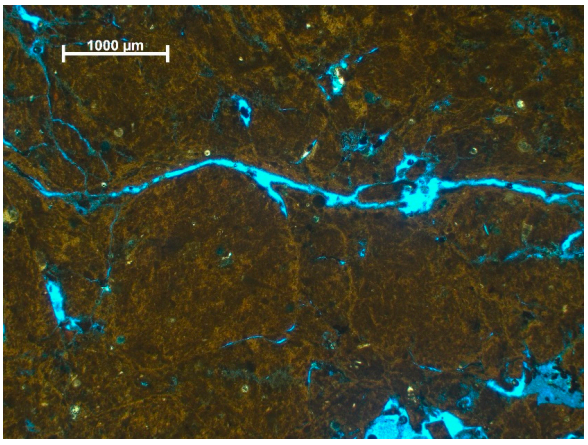

Plate C97. Detail of 'clasts' defined within the bentonite by the shear network. Porosity is beginning to develop along this network.

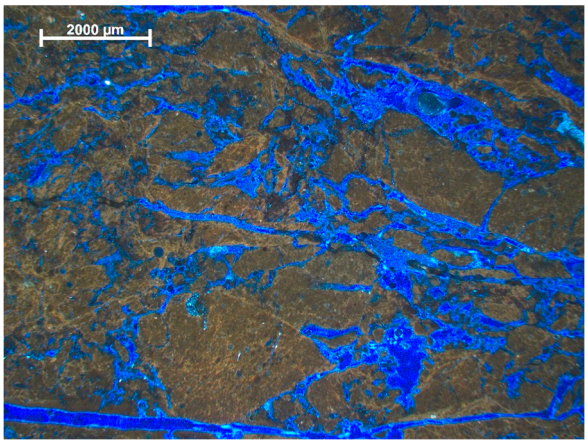

Plate C98. PPL image from the more fractured, left side of the thin section. The material has largely been split into smaller clasts, and only a few examples of the network of fine shear planes remains.

3.17.3. SEM Analysis

The shear network is not visible under the SEM indicating there is no chemical change in the material. However, the developing network of micro fractures is clearly visible, illustrating the development of the 'chicken-wire' texture and pellets within the bentonite (Plate C99). The bulk of the matrix is very fine-grained (clasts <30 µm). Microfossils are extremely rare. A few small mm

patches of slightly coarser material (clasts <80 μm) were identified within this fine-grained bentonite (Plate C100).

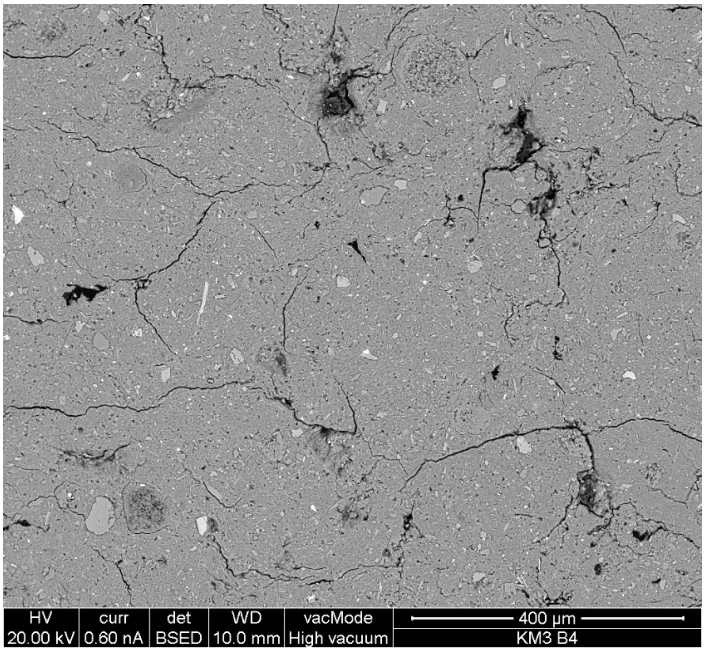

Plate C99. BSEM image showing the development of the 'chicken-wire' texture defined by micro fractures. The anastomising network of fine shear planes is not apparent, indicating there is no chemical change.

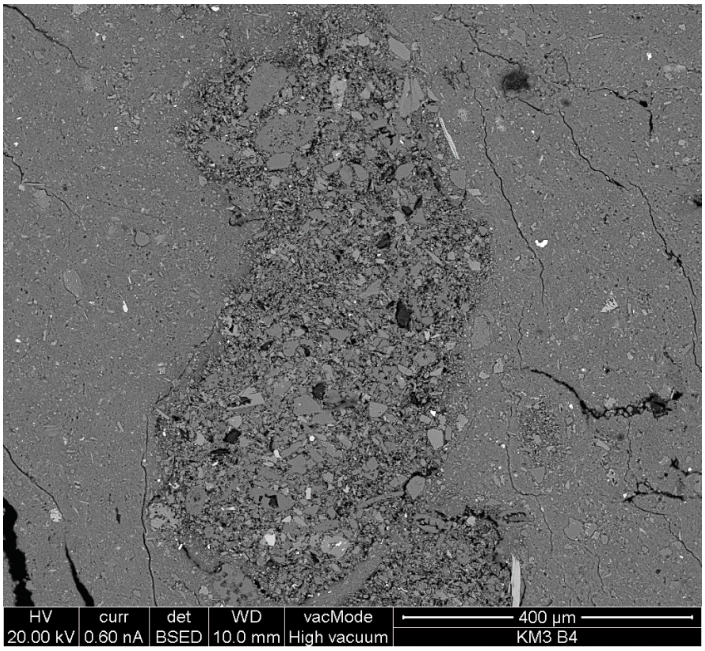

Plate C100. BSEM image of a small patch of coarser material within the fine-grained bentonite.

3.18. KM3 B5

3.18.1. Hand Sample

A light, pinkish-brown bentonite with rare patches of beige material. Some sub-horizontal fracturing was visible on the outer core. The sample remained competent after splitting, but the internal texture was reasonably rough indicating fracturing is present within the sample.

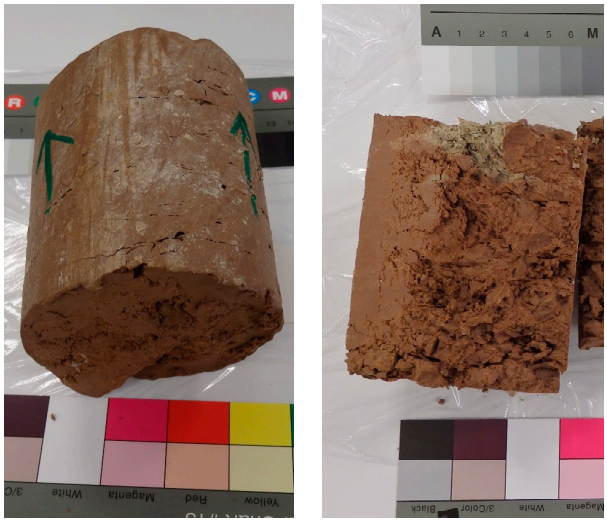

Plate C101. Photographs of the hand sample. **Left**: the sample prior to cutting; **Right**: half of the cut sample showing the internal texture.

3.18.2. Optical Analysis

Numerous listric faults and sygmoidal fractures are visible in the thin section scan (Plate C102). The resulting clasts are angular to sub-rounded. There are changes in fracture pattern throughout the thin section, reflecting the localised shear strain (Plate C103). Some limited development of a pelleted or 'chicken-wire' texture is present, with some pellets being clearly defined by curved fractures which contrast to the dominant angular fractures throughout the sample (Plate C104). Towards the top left of the section, a 'polka-dot' texture is present with numerous small light coloured spheres (<100 μm) visible (Plate C105).

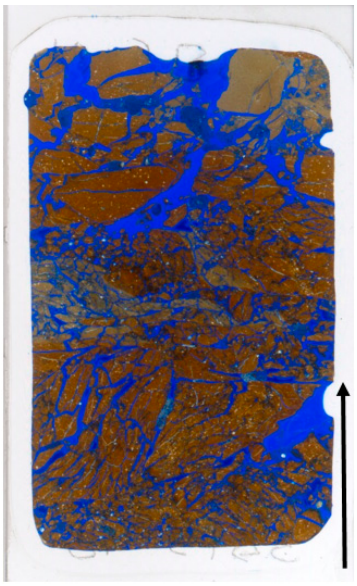

Plate C102. Scanned image of the thin section showing way-up orientation.

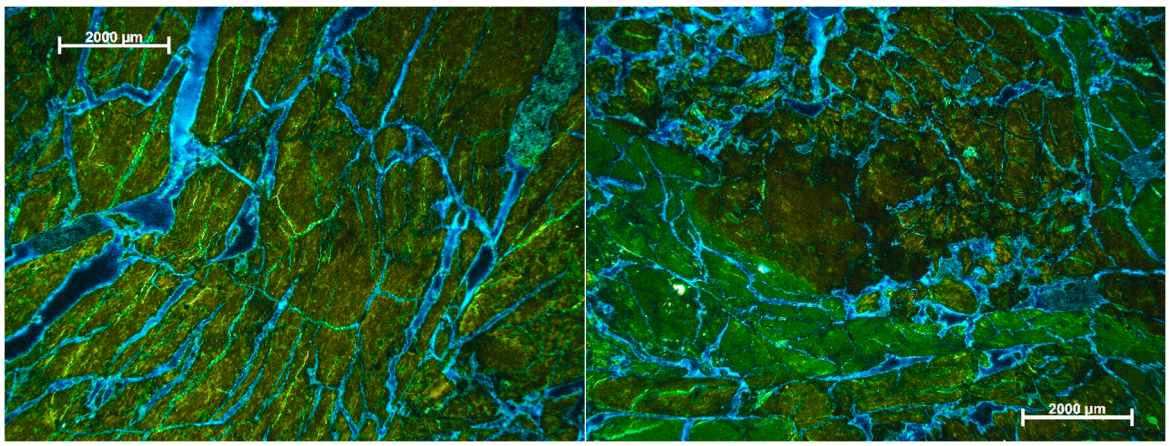

Plate C103. PPL images showing two examples of different localised fracture patterns. **Left**: the fracturing is dominated by regular, elongate, sub-vertical fractures; whereas **Right**: the fractures are shorter and more sub-horizontal dominated.

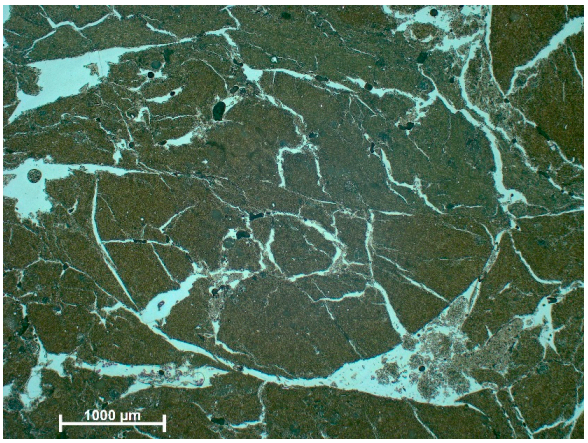

Plate C104. Reflected light image showing a curved fracture defining a pellet. 'Pelletisation', or development of a 'chicken-wire' texture is present but minor in this sample.

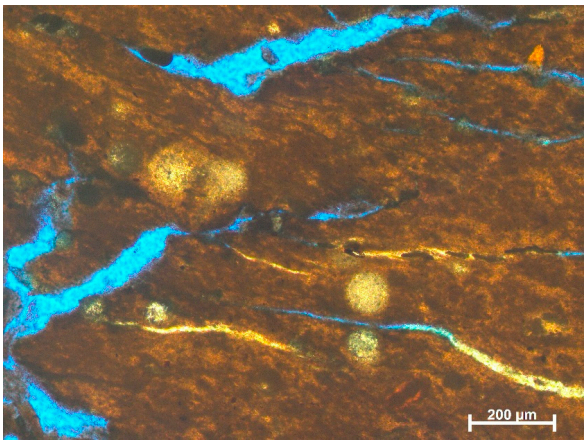

Plate C105. PPL image of the 'polka-dot' texture present in the top-left of the thin section.

3.18.3. SEM Analysis

The bentonite is extremely fine grained (grains <20 µm) and micro fossil-free. The polka-dots are clusters of Si-rich rims with porous centres (Plates C106 and C107). These features are probably a diagenetic texture resulting from the breakdown of bacteria or micro-organisms, and are probably a

zeolitic composition. Micro fractures have propagated around these polka-dots, indicating that the rims are more competent than the surrounding bentonite.

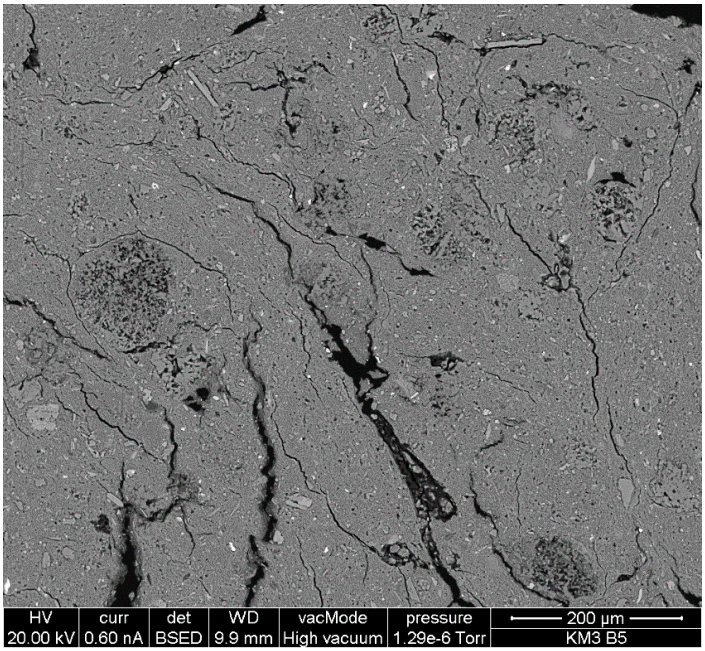

Plate C106. BSEM image of the 'polka-dot' texture showing the 'polka-dots' with their Si-rich rims and porous centres. Note the propagating of the micro fractures around the 'polka-dots'.

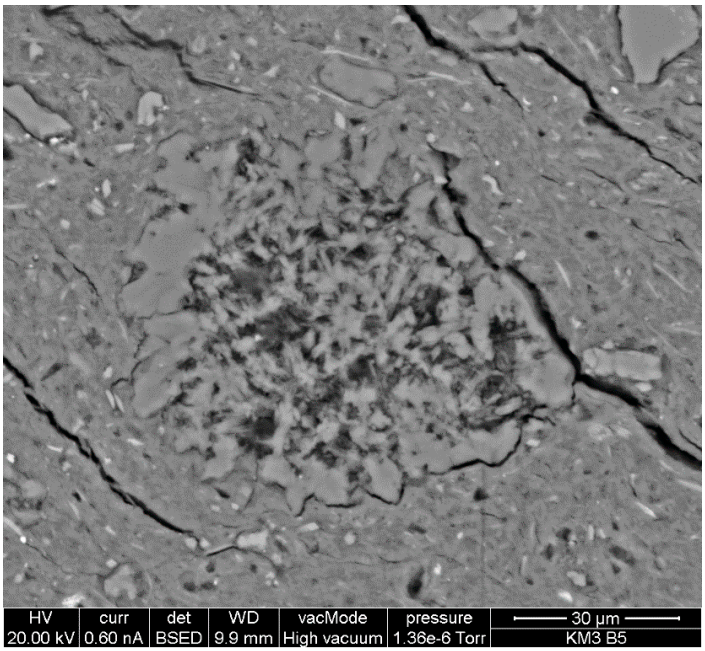

Plate C107. BSEM image showing a 'polka-dot' in detail. The Si-rich rim and porous centre are clearly visible. Note the pathway of the propagating micro fractures.

3.19. KM3 B6

3.19.1. Hand Sample

The sample is a mid-brown, homogenous, fine grained bentonite. Sub-horizontal fractures were present on the outer core. This sample split smoothly and remained competent. Sinuous, lighter brown coloured patches were visible on the interior surface of the split core.

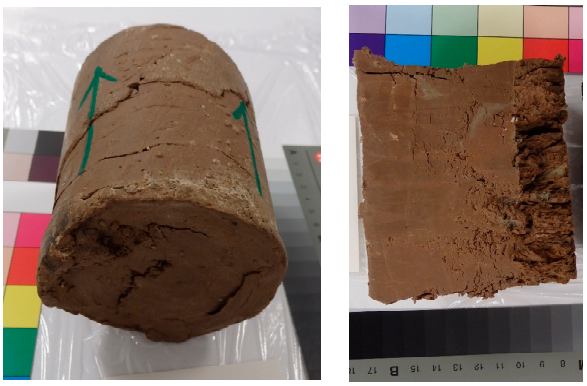

Plate C108. Photographs of the hand sample. **Left**: the sample prior to cutting; **Right**: half of the cut sample showing the internal texture.

3.19.2. Optical Observations

This sample is less fractured than previous samples from this borehole. The section is divided into subhorizontal 'packets' of material defined by an extensive network of fine shear planes. These subhorizontal 'packets' contain angular fractures. A similar network of fine, lighter coloured shear planes is present, although there is a less developed 'chicken-wire' texture, and less development of porosity and fracturing along the shear plane network. The 'polka-dot' texture observed in sample KM3 B5 is more pronounced in this sample.

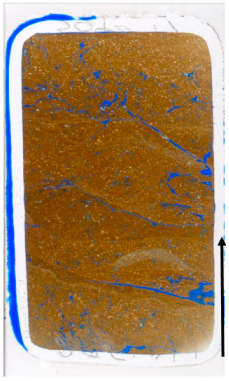

Plate C109. Scanned image of the thin section showing way-up orientation.

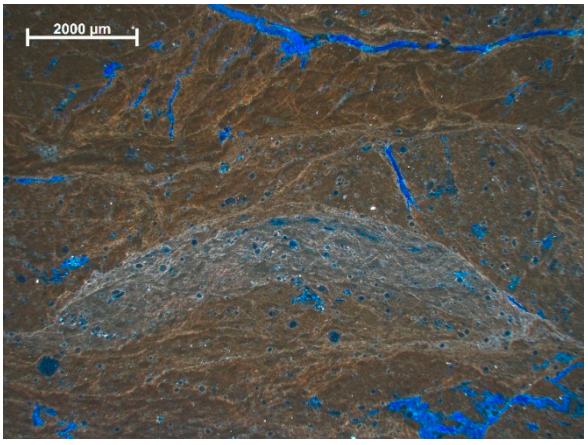

Plate C110. PPL image showing the extensive network of lighter coloured shear planes which sub divide the thin section into sub-horizontal 'packets' of material. Each 'packet' contains a number of angular fractures.

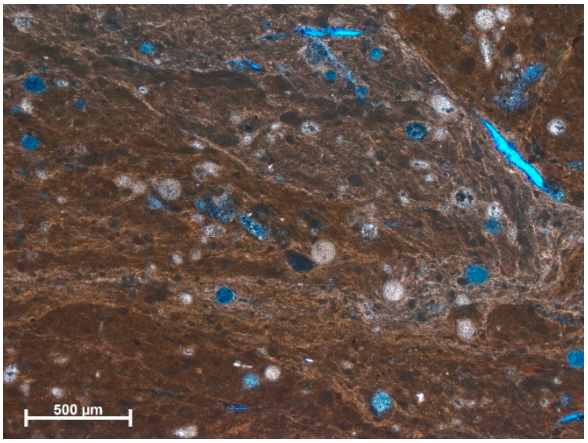

Plate C111. PPL image showing the 'polka-dot' texture, together with the extensive shear plane network.

3.19.3. SEM Analysis

The shear plane network is not apparent under backscatter imaging indicating there is no chemical alteration. However, there are extensive micro fractures which probably correlate to the shear planes, and are the beginning of fracture and porosity development (as observed in KM3 B5: Plate C112). The 'polka-dots' vary in porosity; some are quite dense with low porosity whilst others have very porous interiors (Plate C113). The bentonite in this sample is extremely fine grained with clasts generally too fine to define. However, there are rare patches of coarser grained material, with clasts <20 µm (Plate C114).

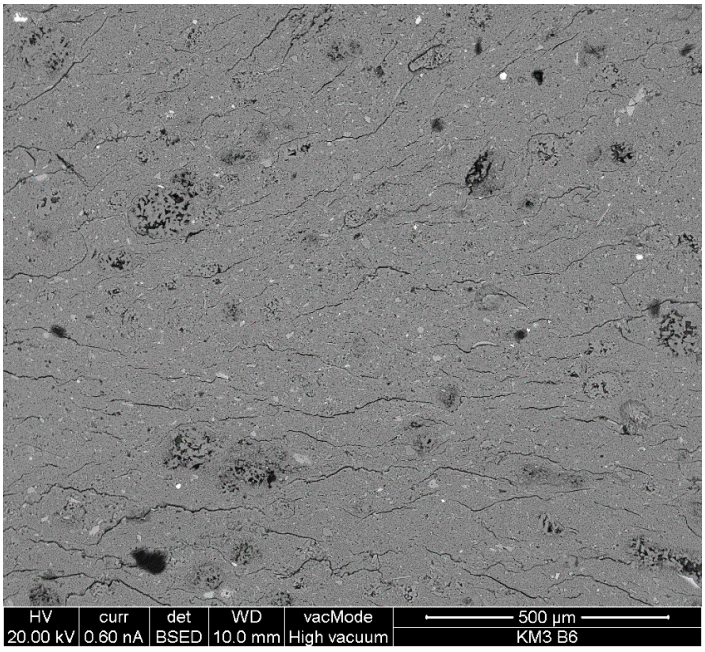

Plate C112. BSEM image showing a network of porous 'polka-dots' and micro fractures. The micro fractures change preferential orientation from oblique (in the upper half of the image) to horizontal (in the lower half of the image).

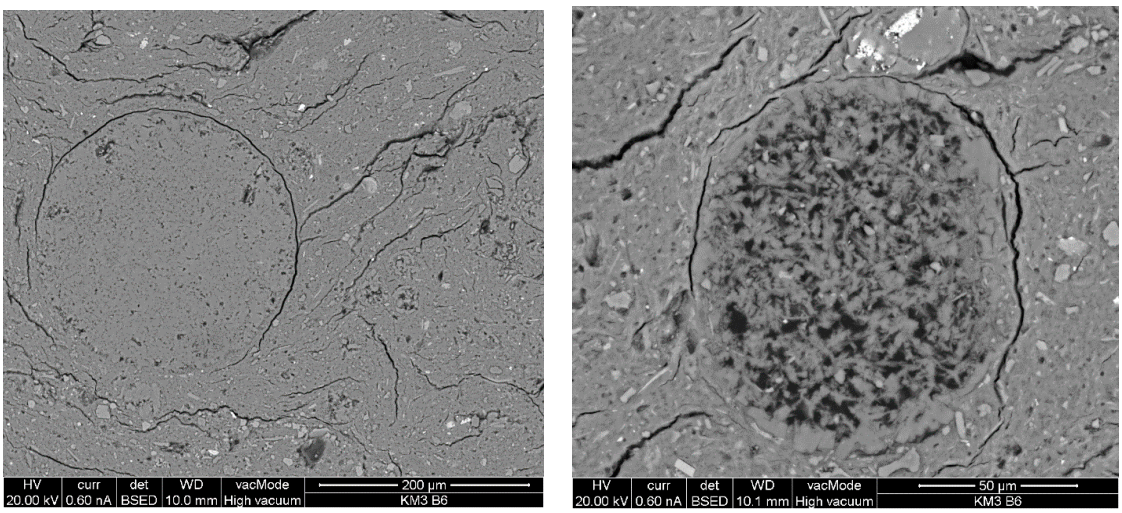

Plate C113. BSEM images of two examples of 'polka-dots'. **Left**: a dense 'polka-dot' defined by a near-perfect circular fracture; **Right**: a more porous 'polka-dot' surrounded by a series of micro fractures.

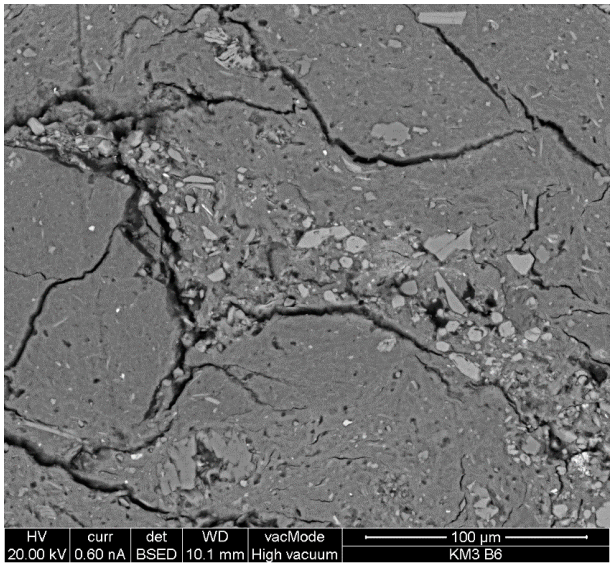

Plate C114. BSEM image showing the texture of the bentonite. The bulk is extremely fine grained (grains generally too fine to define), but there are rare patches of coarser material (grains <20 µm). Micro fractures ae widespread.

3.20. KM3 B7

3.20.1. Hand Sample

A dark brown, fine-grained, smooth core, free of fractures in the outer core. Following splitting, the interior was distinctly banded with sub-horizontal bands of very dark brown, and slightly lighter brown. The split surface was reasonably rough.

Plate C115. Photographs of the hand sample. **Left**: the sample prior to cutting; **Right**: half of the cut sample showing the internal texture.

3.20.2. Optical Observations

The sample is compartmentalised into localised zone of shear. Shear and slip planes are varyingly, listric, sigmoidal as well as Anderson type conjugate pairs. Fracturing and porosity is developing along these shear planes, although fractures and porosity is less well developed than in samples KM3 B5 and B6. The bentonite is fine grained with an absence of micro fossils.

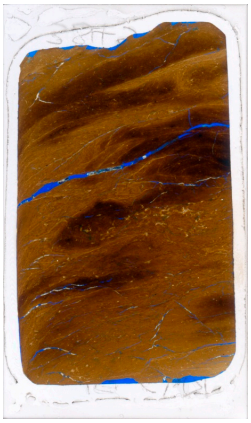

Plate C116. Scanned image of the thin section. The way-up orientation is unknown.

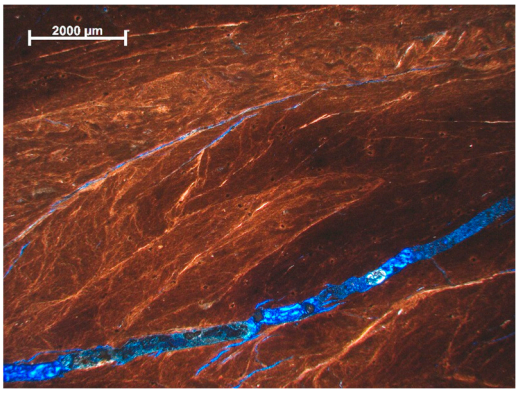

Plate C117. PPL image showing listric and sigmoidal shear planes visible within the fine-grained bentonite. Fractures and micro fractures can be seen developing along these planes.

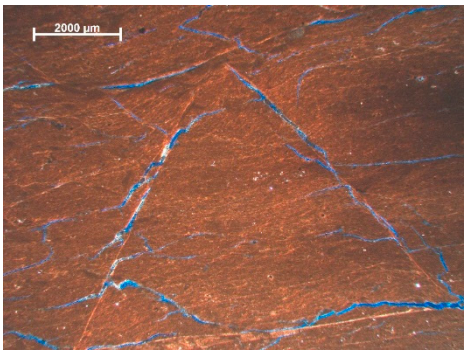

Plate C118. A pair of conjugate shear planes, along which a network porosity and fractures are developing.

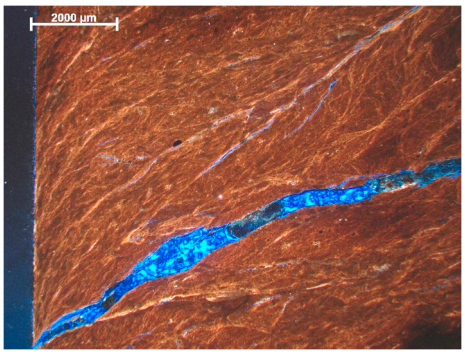

Plate C119. PPL image of the edge of the section. Shear planes and fractures curve towards the edge of the section. This may be an artefact of the drilling process.

3.20.3. SEM Analysis

KM3 B7 is very similar to KM3 B5 and B6 in that a network of fine micro fractures reflect the network of shear planes observed under optical microscopy. Microfractures reflect S and C type folia, indicating the sample has been subjected to dextral shear. The bentonite is fine grained (<10 µm) with occasional coarser clasts. The 'polka-dot' textures observed in the previous samples is absent here. Occasional thin bands (<50 µm deep) of fine grained, material, slightly higher in Mg than the matrix are present.

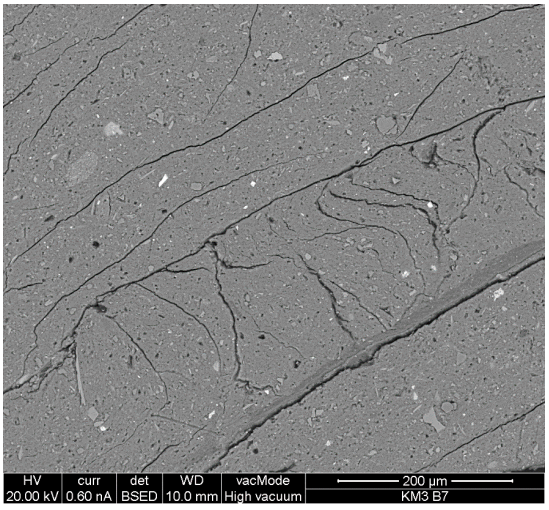

Plate C120. BSEM image showing the network of micro fractures with a band of well-developed S and C type folia, reflecting dextral shear. Not the differing orientation of micro fractures which reflect the differing local shear in each 'packet'. Note the thin, oblique and slightly darker band in the lower right quadrant. This is slightly higher in Mg content than the surrounding matrix.

4. Physical Properties of Bentonite from the Kato Moni Cores

Table S4. Physical properties of bentonite from cores KM1, KM2, KM3 and KM3a plus a few additional samples of interest.

Sample	Depth (m)	Atterberg Limits			UCS					Sp Grav.	Methyl. Blue (g/kg)	Sw Press (kPa)	UU Triaxial	
		LL (%)	PI (%)	Shrinkage (%)	MC (%)	MC (%)	BD (g/cm³)	DD (g/cm³)	qu (kPa)				Cohesion (kPa)	ϕ°
KM1														
B1+	8.40–8.55	62	37	14	14.6					2.860				
B3-1	9.08–9.17				26.5	29.4	1.84	1.42	219					
B3-2	9.17–9.30									2.592				
B3-3	9.50–9.60					22.4	1.85	1.51	361					
B4-1	9.80–10.10				24.4		1.87						172	22
B5-1	10.20–10.42									2.553				
B6-1	10.60–10.70					27.9	1.85	1.45	-	2.487		166.1		
B6-2	10.84–11.16				28.4		1.86	1.45					109	18
B6-3	11.16–11.55	84	59	21	28.6		1.82	1.41		2.674	92.3	196.6	93	17
					29.0		1.88	1.46					50	12
3: trial hole next to KM1														
	9.50–9.80				26.4		1.72	1.36					140	18
	9.82–10.05	89	60	22	29.0	29.2	1.82	1.41	299	2.679	100.7	109.8		
	10.15–10.42	88	65	19	28.1	27.9	1.88	1.47	486		110.0	126.8		
	10.82–10.98	86	58	19	29.6	28.3	1.85	1.44	369		96.7			
	11.00–11.60	100	71	21	29.7	30.5	1.76	1.35	273		122.3	195.5	130	21
	11.60–12.20	106	71	23	31.3	31.2	1.81	1.38	440	2.719	118.3	309.2	202	21
													190	19
	12.20–13.20	86	63	21	30.5	29.2	1.88	1.45	275	2.861	97.3	287.9	107	18
	12.85–13.05					29.0	1.86	1.44	305					
KM2														
B3-1	13.82–14.05					23.0	1.91	1.55					205	19
B3-2	14.20–14.40	113	93	16	23.5	23.5	1.91	1.55	481	2.685	130.0	188.6		
2D: trial hole next to KM2														
	15.0–15.25					21.4	1.92	1.58	581					
KM3a														
B1-1	0.35–0.54	132	103	23	21.2	22.4	1.34	1.09	-	2.719	146.7	147.5		
B3-1	0.95–1.30	115	89	26	29.9		1.67	1.29		2.617	127.3	228.9	25	12

B3-2	1.30–1.52					34.6	1.66	1.23	237					
B4-1	1.70–1.84	107	81	21	30.3						119.0	284.8		
B4-2	1.84–1.97					31.3	1.59	1.21	174					
B5-1	2.20–2.26											367.3		
B5-2	2.26–2.44	109	84	20		30.7	1.70	1.30	219	2.570	121.7			
B5-3	2.44–2.80	109	83	19	34.1	34.3	1.65	1.23	-	2.565	124.0	345.0	105	13
KM3b														
B6	3.00–3.23				27.1	27.1	1.61	1.27	127					
B6-sub	4.00–4.20	112	80	22	26.9		1.62	1.28		2.542	124.0	205.6	63	13
1A: trial hole next to KM3														
	0.02–0.12											156.4		
	1.00–1.45				31.2		1.65	1.26					95	11
	1.45–1.73	114	79	22	31.8		1.73	1.31		2.570	161.7	255.2	18	9
	1.73–2.00	107	85	29		32.5	1.74	1.31	395	2.587	152.3	219.9		
	2.01–2.50	108	81	21	29.9	28.8	1.72	1.34	-	2.499	122.3	186.7	85	15
	2.50–2.65	113	88	22						2.655	134.0	195.5		

5. Natural Decay Series Data for Kato Moni Core Samples KM1, KM2 and KM3

Table S5. Alpha-spectroscopy results for samples from cores KM1, KM2 and KM3. Uncertainties represent 1σ total error.

Sample	^{232}Th	^{230}Th	^{238}U	^{235}U	^{234}U	^{234}U/^{238}U	^{230}Th/^{234}U	^{230}Th/^{238}U
	Bq·kg^{-1}	Bq·kg^{-1}	Bq·kg^{-1}	Bq·kg^{-1}	Bq·kg^{-1}			
KM1								
KM1-L1	1.35 ± 0.09	5.31 ± 0.21	3.52 ± 0.14	0.16 ± 0.03	3.86 ± 0.15	1.10 ± 0.06	1.37 ± 0.08	1.51
KM1-B1	2.32 ± 0.34	9.11 ± 0.74	8.62 ± 0.23	0.33 ± 0.04	9.14 ± 0.24	1.06 ± 0.04	1.00 ± 0.08	1.06
KM1-B2a	2.58 ± 0.27	12.29 ± 0.69	9.48 ± 0.42	0.46 ± 0.09	9.63 ± 0.42	1.02 ± 0.06	1.28 ± 0.09	1.30
KM1-B3	2.02 ± 0.49	9.13 ± 1.14	7.81 ± 0.26	0.27 ± 0.05	8.15 ± 0.27	1.04 ± 0.05	1.12 ± 0.14	1.17
KM1-B4	2.87 ± 0.35	10.45 ± 0.75	8.5 ± 0.29	0.28 ± 0.05	9.68 ± 0.31	1.14 ± 0.05	1.08 ± 0.08	1.23
KM1-B7	BDL	21.99 ± 3.17	11.4 ± 0.24	0.44 ± 0.04	11.18 ± 0.24	0.98 ± 0.03	1.97 ± 0.29	1.93
KM2								
KM2-B1	2.34 ± 0.54	12.16 ± 1.38	8.16 ± 0.22	0.33 ± 0.04	9.20 ± 0.24	1.13 ± 0.04	1.32 ± 0.15	1.49
KM2-B3	1.83 ± 0.48	11.67 ± 1.36	7.85 ± 0.45	0.30 ± 0.08	9.23 ± 0.49	1.18 ± 0.09	1.26 ± 0.16	1.49
KM2-B4	1.93 ± 0.46	11.41 ± 1.25	8.71 ± 0.20	0.31 ± 0.04	9.61 ± 0.21	1.10 ± 0.03	1.19 ± 0.13	1.31
KM2-B6	2.41 ± 0.62	12.32 ± 1.57	11.86 ± 0.26	0.51 ± 0.05	11.97 ± 0.26	1.01 ± 0.03	1.03 ± 0.13	1.04
KM2-B7	1.98 ± 0.48	8.33 ± 1.07	8.72 ± 0.38	0.3 ± 0.07	8.85 ± 0.38	1.01 ± 0.06	0.94 ± 0.13	0.96
KM3								
KM3-B1	BDL	BDL	27.05 ± 0.68	1.22 ± 0.12	26.05 ± 0.66	0.96 ± 0.03	-	-
KM3-B2	37.72 ± 5.24	28.44 ± 4.23	17.82 ± 0.64	0.75 ± 0.12	16.69 ± 0.61	0.94 ± 0.04	1.71 ± 0.26	1.60
KM3-B3	14.89 ± 1.47	22.42 ± 1.94	14.4 ± 0.58	0.63 ± 0.11	14.29 ± 0.57	0.99 ± 0.05	1.57 ± 0.15	1.56
KM3-B5	26.05 ± 3.69	13.16 ± 2.32	13.62 ± 0.52	BDL	13.14 ± 0.51	0.96 ± 0.05	1.00 ± 0.18	0.97

BDL: below detection limit.

Table S6. Gamma-spectroscopy results for samples from cores KM1, KM2 and KM3. Uncertainties represent 1σ total error.

Sample	Uranium Series Bq·kg^{-1}						Thorium Series Bq·kg^{-1}		
	^{210}Pb (46keV)	^{234}Th (63 keV)	^{214}Pb (295 keV)	^{214}Pb (352 keV)	^{214}Bi (609 keV)	^{226}Ra *	^{212}Pb (239 keV)	^{208}Tl (584 keV)	^{228}Ac (911 keV)
KM1									
KM1-L1	BDL	7 ± 2	BDL	4 ± 2	BDL	4 ± 2	BDL	BDL	9 ± 6
KM1-B1	11 ± 3	12 ± 3	BDL	6 ± 2	4 ± 3	5 ± 3	2 ± 1	BDL	BDL
KM1-B2a	13 ± 3	12 ± 2	BDL	9 ± 2	8 ± 3	9 ± 3	2 ± 1	5 ± 4	7 ± 6
KM1-B3	8 ± 2	9 ± 2	BDL	4 ± 2	6 ± 3	5 ± 3	BDL	BDL	BDL
KM1-B4	15 ± 3	20 ± 3	BDL	12 ± 2	9 ± 3	11 ± 3	3 ± 1	6 ± 5	10 ± 7
KM1-B7	7 ± 6	8 ± 6	11 ± 2	10 ± 1	14 ± 2	12 ± 2	5 ± 1	14 ± 2	17 ± 3
KM2									
KM2-B1	8 ± 2	13 ± 2	BDL	7 ± 2	9 ± 3	8 ± 3	BDL	7 ± 4	BDL
KM2-B3	9 ± 2	8 ± 2	BDL	10 ± 2	4 ± 3	7 ± 3	BDL	5 ± 4	BDL
KM2-B4	12 ± 3	15 ± 3	BDL	12 ± 2	6 ± 3	9 ± 3	BDL	BDL	7 ± 6
KM2-B6	14 ± 2	13 ± 2	BDL	12 ± 2	13 ± 3	13 ± 3	BDL	7 ± 4	BDL
KM2-B7	9 ± 3	15 ± 3	BDL	8 ± 2	8 ± 3	8 ± 3	BDL	6 ± 4	BDL
KM3									
KM3-B1	10 ± 2	22 ± 2	BDL	17 ± 2	14 ± 3	16 ± 3	16 ± 1	31 ± 4	BDL
KM3-B2	13 ± 2	19 ± 2	5 ± 3	19 ± 2	20 ± 3	20 ± 3	19 ± 1	13 ± 4	BDL
KM3-B3	9 ± 2	15 ± 2	5 ± 3	11 ± 2	18 ± 3	15 ± 3	16 ± 1	18 ± 4	BDL
KM3-B5	9 ± 6	10 ± 6	10 ± 2	11 ± 1	13 ± 1	12 ± 1	21 ± 1	35 ± 2	33 ± 2

* ^{226}Ra component calculated from the average of the 352 keV and 609 keV photopeaks; BDL: below detection limit.

Table S7. Natural decay series disequilibria results for samples from cores KM1, KM2 and KM3. Note here uncertainties represent 2σ total error.

Sample	$^{234}U/^{238}U$	$^{230}Th/^{234}U$	$^{230}Th/^{238}U$	$^{226}Ra/^{230}Th$
KM1				
KM1-L1	1.10 ± 0.12	1.37 ± 0.16	1.51 ± 0.17	0.75 ± 1.89
KM1-B1	1.06 ± 0.08	1.00 ± 0.16	1.06 ± 0.16	0.54 ± 2.24
KM1-B2a	1.02 ± 0.12	1.28 ± 0.18	1.30 ± 0.09	0.73 ± 0.31
KM1-B3	1.04 ± 0.10	1.12 ± 0.28	1.17 ± 0.22	0.64 ± 0.96
KM1-B4	1.14 ± 0.10	1.08 ± 0.16	1.23 ± 0.13	1.05 ± 0.54
KM1-B7	0.98 ± 0.06	1.97 ± 0.58	1.93 ± 0.15	0.54 ± 0.82
KM2				
KM2-B1	1.13 ± 0.08	1.32 ± 0.30	1.49 ± 0.16	0.66 ± 1.19
KM2-B3	1.18 ± 0.18	1.26 ± 0.32	1.49 ± 0.17	0.60 ± 1.48
KM2-B4	1.10 ± 0.06	1.19 ± 0.26	1.31 ± 0.17	0.79 ± 0.89
KM2-B6	1.01 ± 0.06	1.03 ± 0.26	1.04 ± 0.25	1.05 ± 0.50
KM2-B7	1.01 ± 0.12	0.94 ± 0.26	0.96 ± 0.28	0.96 ± 0.82
KM3				
KM3-B1	0.96 ± 0.06	-	-	-
KM3-B2	0.94 ± 0.08	1.71 ± 0.52	1.60 ± 0.19	0.70 ± 0.60
KM3-B3	0.99 ± 0.10	1.57 ± 0.30	1.56 ± 0.12	0.67 ± 0.65
KM3-B5	0.96 ± 0.10	1.00 ± 0.36	0.97 ± 0.37	0.91 ± 0.43